Check for updates

Fabrication and characterization of NiCu/GO and NiCu/rGO nanocomposites for fuel cell application†

Aya Mohamed,[a] Mohamed Shaban, *[b] Mohamed G. M. Kordy, *[ac] Ghadah M. Al-Senani,[d] M. F. Eissa[a] and Hany Hamdy[a]

This study investigated the electrochemical behavior of NiCu, NiCu/GO, and NiCu/rGO nanocomposites designed by combining a modified Hummers' method and hydrothermal technique. The prepared nanocomposites are tested as electrocatalysts in direct alcohol oxidation fuel cells (DAFCs) to identify the role of GO and rGO as catalyst supports for the enhancement of the NiCu composite performance. The production of the NiCu/GO and NiCu/rGO composites was demonstrated by FTIR spectroscopy, EDX, and SEM analyses. In DAFCs experiments, NiCu/rGO has better catalytic activity than pure NiCu and NiCu/GO composites, whereas the use of rGO and GO as supports enhances the performance of NiCu by 468.2% and 377.7% in methanol and 255.6% and 105.9% in ethanol, respectively. The higher performance was caused by the increased density of active dots and the combined electronic effects in the designed catalysts. The stabilities of the catalysts and charge carriers' dynamics are studied using chronoamperometry and electrochemical impedance spectroscopy.

1. Introduction

Both the existence of humans and the prosperity of the economy depend on energy. Rapid industrial and technological development with increasing world population requires a lot of energy for a modernized society. To meet the rising need for energy, fossil fuels are used. However, they are also the main source of CO_2, NO_2, and other dangerous air pollutants that cause acid rain, ozone depletion, and climate change.[1] In this case, renewable energies such as wind and solar power could be a great option; however, they may not be enough to supply the growing need for energy. Therefore, there is a growing focus on finding sustainable energies.

Recently, fuel cells (FCs) have drawn more interest as an alternative fuel and a potential solution for producing clean energy.[2] Depending on the used fuels and membranes, FCs can be categorized into solid oxide, phosphoric acid, polymer electrolyte membrane, molten carbonate, alkaline, and direct alcohol cells.[3] Designing electro-catalysts is the main focus for the electrooxidation of a direct alcohol fuel cell (DAFC), which is a potential source of energy due to the high energy densities of the alcohols (methanol, ethanol, *etc.*) it uses. DAFC has many advantages for the power industry, such as high efficiency, easy transportation and storage of liquid fuel, low noise, and simple maintenance.[4] Despite these possible benefits, the anode catalyst's high cost and limited electrocatalytic performance are significant issues.[5] Thus, a lot of focus has been placed on the development of anodic catalysts and engineering structural perspectives to produce a catalyst with high electrocatalytic activity, stability, and affordability.

Without a doubt, Pt is considered an effective catalyst for ethanol/methanol electrooxidation reactions; however, its application has been restricted because of its expensive price, the scarcity of noble metals, and the decline in performance brought on by reactive intermediate poisoning.[6,7] Therefore, to address these issues, different alloys from Pt with Ru, Pd, and Sn were employed to increase the electrocatalytic activities and lower costs; however, they suffer greatly from heavy aggregation.[8,9] To address this issue, nickel (Ni) metal is the most commonly used anodic catalyst because of its affordable price, significant electrocatalytic efficiency, and selectivity. Nevertheless, Ni electrocatalysts are quite prone to being inactive by carbon deposition and sintering during long-term usage, both of which can result in diminished cell performance.[10,11] Adding moisture to the supply streams can help to mitigate the carbon

aNanophotonics and Applications Lab, Physics Department, Faculty of Science, Beni-Suef University, 62514, Beni-Suef, Egypt. E-mail: ayaelkhatib22@gmail.com; m. kordybio@science.bsu.edu.eg; mostafa.eisa@science.bsu.edu.eg; hshamdy@hotmail.com

bDepartment of Physics, Faculty of Science, Islamic University of Madinah, 42351, Madinah, Saudi Arabia. E-mail: mssfadel@aucegypt.edu

cBiochemistry Department, Faculty of Science, Beni-Suef University, Beni-Suef 62521, Egypt

dDepartment of Chemistry, College of Science, Princess Nourah bint Abdulrahman University, P.O. Box 84428, Riyadh 11671, Saudi Arabia. E-mail: gmalsnany@pnu.edu.sa

† Electronic supplementary information (ESI) available. See DOI: https://doi.org/10.1039/d3ra07822a

deposition constraint. Nevertheless, it has been observed that to avoid carbon deposition, a very high steam-to-carbon ratio is needed. The elevated steam ratio has the potential to worsen the cell electrical performance, dilute the fuel, and oxidize the Ni electrocatalyst.

Alternatively, by enhancing the catalytic activity of various metal-based electrocatalysts, for example, Ni/Cu alloys, the DAFC anodes' catalytic stability and coke resistance can be improved.[12] Ni and Cu are face-centered cubic metals of very close lattice parameters (α = 3.523 and 3.616 Å, respectively). Hence, Ni–Cu alloys may be made in a broad range of compositions. The chemical and physical properties of Ni–Cu alloys have been covered in many published works. Danaee et al.[13] provided an outstanding analysis of the behavior of Ni–Cu alloys in the hydrogenation reaction. In addition, Ni/Cu alloys exhibited excellent resistance to corrosion and biofouling, and good thermal and electrical conductivities.[14] However, these alloys face a drawback that has to be addressed: they are not very resistant and possess insufficient hardness. Although there is currently a lack of research on Ni/Cu, materials including nano reinforcement have been shown to significantly improve mechanical qualities such as strength, hardness, and wear resistance.[15] Carbon nanotubes (CNT) and GO are two types of nanomaterials that have garnered a lot of interest due to their superior characteristics.[16]

GO is a form of graphene that has been modified with functional groupings that include oxygen. It is typically synthesized by employing strong oxidizing chemicals to oxidize graphite such as potassium permanganate or nitric acid. The resulting material has a layered structure with surface functional groups containing oxygen, making it hydrophilic and easy to disperse in water. It has piqued attention in many scientific domains because of its desirable qualities, such as its strong mechanical strength,[17] electrical conductivity,[18] molecular barrier abilities,[19] and other remarkable properties. GO is a single layer of hexagon-shaped carbon with π-electron clouds and sp^2 hybridization C–C bonds. Mono-layer graphene and other thin flakes consisting of a few layers of C atoms have interesting structural and physical properties that make them potentially useful in a variety of technological disciplines. For these reasons, various research studies have sought to incorporate graphene into nanocomposites. M. Wala et al.[20] prepared the NiCuGO electrocatalyst using electrodeposition for methanol oxidation, which had a high current density of 28.6 mA cm^{-2}. However, it needed more optimization to improve the activity and stability of the nanoscale catalyst. The NiCuGO electrocatalysts, used by M. Wala et al.,[21] also achieved a current density of 10 mA cm^{-2} at 0.693 V in 0.15 M urea in 1 M KOH. However, the composite catalyst produced more nitrite and ammonia ions from urea oxidation, as shown by reaction product analysis. Additionally, B. M. Thamer et al.[22] observed a high current density of 140 mA cm^{-2} at 0.34 V using the NiCu@ porous carbon nanosheets electrocatalyst. S. Gupta and M. De found that the 20Ni-carbon catalyst had the highest current density (11 mA cm^{-2} at 1 V in basic medium) and structural stability among the tested Cu, Ni, Co, or Fe-carbon composite catalysts for the electro-oxidation of ethylene glycol.[23] The work was well-supported by a detailed analysis of the catalysts, but it did not consider other fuels such as methanol or ethanol, nor did it reach a current density that would be suitable for industrial applications.

According to most sources, reduced graphene oxide (rGO) is the favored material amongst graphite, graphene, and graphene oxide.[24] rGO is more stable in solvents than graphene or graphite. Also, it does not clump together and may be stored for extended periods. rGO is also substantially more conductive and robust than graphene oxide.[25] It has recently been utilized as a catalyst support in FCs.[26–28] Overall, GO and rGO are two related forms of graphene that have unique characteristics and possible uses in a variety of domains. While both materials have their advantages and disadvantages, they represent a promising area of research for the production of novel nanomaterials with special properties and applications. Therefore, the application of graphene nanosheets with other metallic nanostructures can produce enhanced performance, and can be adapted to produce low-cost catalysts.[29] K. Rahmani and B. Habibi demonstrated that the NiCo/reduced N-GO/carbon ceramic electrode catalyst had the highest electrooxidation activity (88.04 and 64.23 mA cm^{-2} for methanol and ethanol, respectively) and stability, which was attributed to the synergistic effect of the NiCo alloy and reduced N-GO.[30] The strength of this work is the use of a simple and cost-effective method to prepare the catalysts, while the weakness is the lack of comparison with other carbon-based materials such as CNT or carbon black. Table 1 shows the

Table 1 Comparison of the designed NiCu/rGO and NiCu/GO electrocatalysts with the previously reported NiCu-based electrocatalysts for the electrooxidation of methanol

Catalyst	Morphology	Electrolyte	E_{Onset} (mV)	Current (mA)	Catalyst dose	Ref.
NiO/CuO MOF	Nanosheets	1 M NaOH/3 M methanol	400 vs. Ag/AgCl	437	2 mg	31
Ni–Cu hybrid oxides/ mesoporous carbon	Mesoporous ceramics	1 M KOH/2 M methanol	350 vs. Ag/AgCl	182	44 mg	32
NP NiCu	Nanoparticles	1 M KOH/0.3 M methanol	380 vs. Ag/AgCl	11	Thin film	33
Cu/NiCuNWs-220/C	Nanorods	1 M KOH/1 M methanol	—	34.9	6 mg	34
(Ni–Cu) sulfide/MNO$_2$	Nano spherical	0.5 M KOH/1 M methanol	380 vs. Ag/AgCl	70	5 mg	35
Ni–Co-graphene 3.5-15	Nanoparticles	1 M KOH/1 M methanol	251.8	3.5	Thin film	36
NiCu/rGO	Nanospheres on nanosheets	1 M KOH/2 M methanol	−509 vs. Hg/HgCl	267	25 mg	This
NiCu/GO	Nanospheres on nanosheets		−279 vs. Hg/HgCl	110	25 mg	study
NiCu	Nanospheres		377 vs. Hg/HgCl	80	25 mg	

previously reported NiCu nanocomposite-based electrocatalysts for methanol electrooxidation and the values of their key performance indicators.[31–36]

This research seeks to develop and express a more efficient, cheaper, and novel electrocatalyst using Cu, Ni, and GO or rGO as replacements for Pt. Here, NiCu, NiCu/GO, and NiCu/rGO nanocomposites are hydrothermally synthesized, characterized, and examined as electrocatalysts for alcohols electro-oxidation in an alkaline medium to explore the role of GO and rGO as supports for the NiCu composite. The performances of the suggested electrocatalysts are examined in relation to the effects of the electrolyte concentrations, scan rates, and reaction durations. In addition, measurements with electrochemical impedance (ECI) spectroscopy, chronoamperometry (CAM), and cyclic voltammetry (CV) are used to analyze the electrode's performances and stabilities. In FCs applications, the NiCu/rGO ternary nanocomposite is probably going to be helpful as available electrocatalysts.

2. Experimental details

2.1. Synthesis of Ni–Cu/GO and Ni–Cu/rGO

Hummers' method was used in our fabrication of graphene oxide (GO) sheets with some modifications according to Zaaba *et al.*[37] This method involves the mixing and stirring of 100 mL H_2SO_4 and 17 mL H_3PO_4 up to 10 min. After that, the liquid is agitated for 1 h at 200 rpm with one gram of graphite powder added. Then, 6 g of solid $KMnO_4$ was gradually added to the mixture while it was in an ice bath to prevent overheating issues. Throughout the day, this combination was continually stirred. After that, 500 mL of distilled H_2O was added to dilute it, and the mixture was stirred for 30 min at 200 rpm. To remove the additional $KMnO_4$, 6 mL of H_2O_2 was added dropwise under 10 min stirring at 100 rpm. It had an exothermic reaction and cooled in the ice bath. After that, the mixture was spun in a centrifuge for 5 minutes at 4000 rpm to get the desired GO as a pellet. Then, pellets were collected in a beaker and washed with a mixture of distilled H_2O and ethanol (C_2H_5OH) several times every day. To obtain the finely GO powder, it was further filtered, dried at 90 °C for 24 hours, and completely ground.

GO (0.5 g) was added to 50 mL of a well-mixed solution of 0.5 g $NiCl_2 \cdot 6H_2O$ and 0.5 g $CuCl_2 \cdot 2H_2O$ under stirring for 1 h at ambient temperature (AT ~20 °C). Then, the product was sealed in a 150 mL autoclave at 200 °C for 3 hours with 25 mL of 10 M KOH. The formed suspension from the hydrothermal process was filtered and dried at 50 °C for 24 hours, and labeled as the NiCu/GO nanocomposite. Finally, NiCu/rGO was produced by treating the GO powder by adding 30 mL hydrazine hydrate ($H_6N_2 \cdot H_2O$), which resulted in thin sheets of reduced GO (rGO), followed by grinding the produced rGO.[38,39] Then, it was used instead of GO in the above steps for the preparation of the NiCu/GO nanocomposite.

2.2. Characterization of NiCu/GO and NiCu/rGO nanocomposites

The nanomorphologies of the synthesized nanocomposites have been analyzed *via* scanning electron microscope (SEM,

Sigma 500 VP, Carl ZEISS, Baden-Württemberg, Germany). The elemental composition of the nanocomposites was explored by a high-energy dispersive X-ray detector integrated into the SEM device (EDX-SEM, AMETEK, Inc., PA, USA). To determine the functional groups of the nanocomposites, Fourier transform infrared (FT-IR) studies were performed using the Bruker Vertex 70 (Bruker, Leipzig, Germany). The NiCu/GO and NiCu/rGO samples were characterized using a portable i-Raman Plus spectrophotometer (B&W Tek, NJ, USA). Using a 532 nm wavelength, the molecules' vibrations were stimulated. A ten-second exposure was used. Moreover, a double-beam UV/Vis/NIR spectrophotometer (Lambda 950, PerkinElmer Inc., Waltham, MA, USA) has been employed for the optical investigations. We also used the XRD device (Philips X'Pert Pro MRD) from Malvern, UK, to detect the crystallography of the NiCu, NiCu/GO, and NiCu/rGO samples so that we could analyse the peak changes in the XRD studies. The XRD charts were generated by scanning the 2 Theta range from 10° to 80° at a rate of 0.01° s^{-1} with Cu-Kα radiation ($\lambda = 0.154\ 056$ nm) operating at 40 kV and 40 mA.

2.3. Electrochemical (EC) analysis

Utilizing an EC workstation (CHI 660E, Austin, TX, USA), the EC studies were conducted by a cell with three electrodes: Pt counter electrode, Hg/HgCl reference electrode, and working electrode (NiCu/rGO or NiCu/GO). For working electrode preparation, 25 milligrams of the produced nanocomposite was combined with 30 microliters of Nafion and 0.4 milliliters of $(CH_3)_2CHOH$. A homogeneous nanocatalyst ink was produced after agitating for one day, then 15 microliters of the ink was injected directly into a glassy carbon electrode with an area of 7.065 mm^2. After that, the electrode was dried at AT (20 °C) for an hour. The voltage was varied from -1 to 1 V *vs.* Hg/HgCl at different scanning rates and varying concentrations of methanol and ethanol. The ECI spectroscopy curves have been obtained at an open circuit voltage of 0.5 V *vs.* Hg/HgCl with a modulation amplitude of 5 mV and a frequency ranging from 100 kHz to 10 Hz. The nanocomposites' catalytic activities were assessed employing polarization curves utilizing linear sweep voltammetry (LSV) at AT with 100 mV s^{-1}.

3. Results and discussions

3.1. Characterizations of the nanocomposites

3.1.1. Morphological study. Fig. 1 depicts the SEM images of the investigated materials and the distribution of particle sizes for NiCu. In Fig. 1(A), the SEM images of NiCu nanoparticles illustrate hexagonal shapes, as seen in the inset images, with the presence of spherical nanoparticles. A narrow size distribution and a high density of nanoparticles are depicted in Fig. 1(B). The mean particle diameter is 43.4 ± 8.1 nm. Fig. 1(C) presents an SEM image showcasing exfoliated GO layers. The image reveals thin, flexible, and wrinkled sheets, which align with the findings reported by Shojaeenezhad *et al.*[40] employing the modified Hummers' method. Notably, the inset in Fig. 1(C) demonstrates that the GO layers are nanolayered.
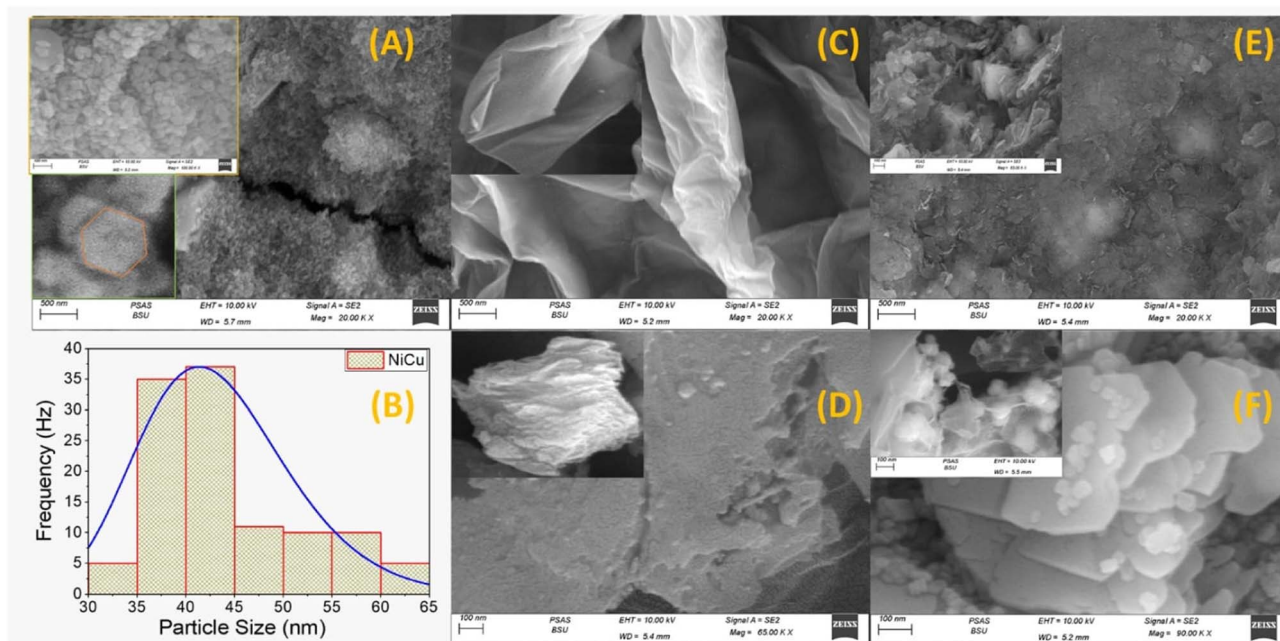
Fig. 1 (A) SEM images of the NiCu nanoparticles and (B) their particle size distribution, and SEM images of the (C) GO, (D) NiCu/GO nanocomposite, (E) rGO and (F) NiCu/rGO nanocomposite.

Fig. 1(D) illustrates the influence of the hydrothermal process on GO nanolayers and NiCu nanoparticles which are impregnated on the GO nanolayers' surfaces, leading to the formation of a compacted and layered nanocomposite material, as shown in the inset. Hence, SEM analysis reveals that the surfaces of the GO nanolayers exhibit rough, textured features due to the accumulation of metallic NiCu nanoparticles, as observed in the distinct shapes present. Fig. 1(E) shows the SEM image of the rGO layers, obtained through the reduction of GO nanolayers using hydrazine hydrate, followed by a subsequent hydrothermal process. The SEM image reveals highly exfoliated sheets of rGO with a rough surface, resembling scales, as

depicted in the inset. Fig. 1(F) presents an SEM image of a nanocomposite consisting of rGO and NiCu nanoparticles. The SEM image reveals condensed nanostructures and nanolayers that appear as nanospheres and polygonal shapes, respectively, suggesting the presence of NiCu nanoparticles encapsulated by rGO blankets, as highlighted in the inset.

3.1.2. Chemical composition and functional groups. The results obtained from the EDX study conducted on pure rGO (Fig. 2(A)) and the NiCu/rGO nanocomposite (Fig. 2(B)) have revealed significant findings regarding their chemical composition. The analysis of the rGO nanosheets demonstrated remarkable properties, including excellent dispersibility and
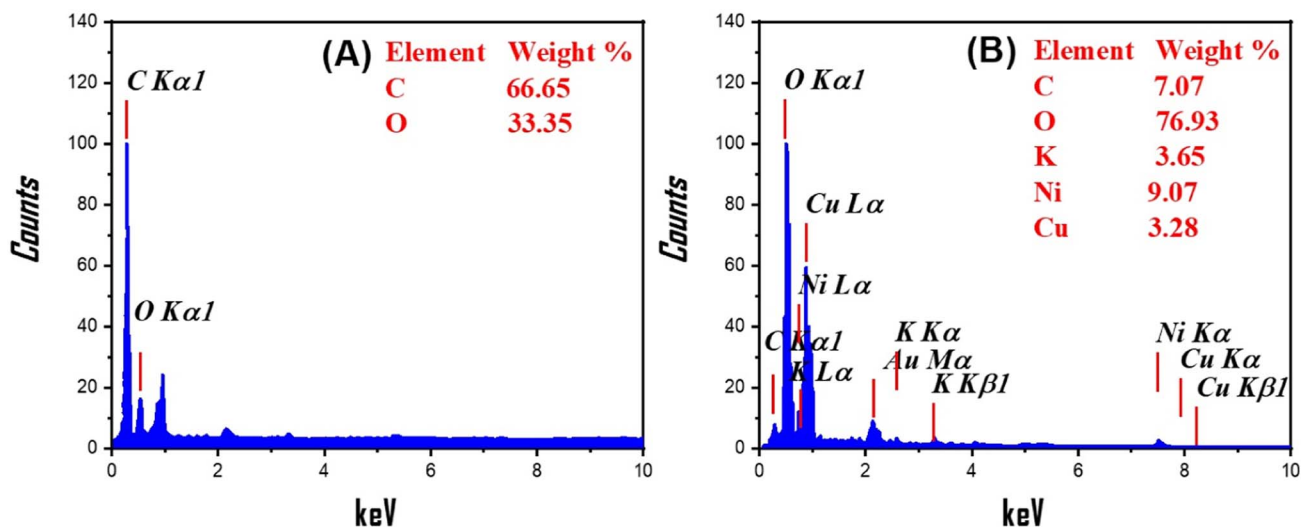

Fig. 2 EDX charts of (A) rGO and (B) NiCu/rGO composite.

a carbon content of 66.65%, along with the presence of oxygen at 33.35%, primarily attributed to the functional groups of carboxylates. These characteristics offer distinct advantages for various applications and facilitate the formation of nanocomposites with other metal ions, showcasing their favorable chemical and structural properties.

Furthermore, the elemental analysis of the NiCu/rGO nanocomposite indicated a reduction in the carbon content to 7.07%, while the oxygen content increased to 76.93%. This shift confirms that the presence of metal ions is associated with the coordination and binding of oxygen, with 9.07% of Ni and 3.28% of Cu being deposited on the surface of the rGO nanosheets. Notably, there was a peak that corresponded to carbon at around 1 keV, while another peak (~1 keV) attributed to both Ni (0.85 keV) and Cu (0.93 keV) exhibited overlapping characteristics, indicating a synthesized rGO nanocomposite composed of Ni and Cu in a 3 : 1 ratio. Additionally, the presence of 3.65% potassium (K) was observed, which can be attributed to the use of KOH during the hydrothermal process for the preparation of the nanocomposite. The presence of gold (Au) signals observed in the SEM-EDX analysis can be attributed to the coating process applied to the sample.

The FTIR analyses shown in Fig. 3 highlight the function groups of the GO, rGO, and NiCu powders in charts (A) and (B) for the NiCu/GO and NiCu/rGO nanocomposites, respectively. They were presented in the wavenumber range of 4000–400 cm^{-1} using the KBr pellets method.

Fig. 3(A) shows significant peaks at 3400, 3433.6, and 3637.8 cm^{-1} that correspond to the O–H bond's stretching mode of the carboxylic group in the case of GO and rGO, and the f–H bond of the produced hydroxides for Ni and Cu in the NiCu sample. The asymmetric stretching vibration of an alkane's C–H bond corresponds to the 2930 and 2854 cm^{-1} peaks in the GO and rGO powders, although it is significantly greater in rGO, confirming the reduction process for GO. The peaks of the GO powder at 1616.9, 1413.4, and 1103.9 cm^{-1} may be attributed to the C=O, C=C, and C–H bonds, correspondingly. The rGO powder exhibits strong and intense peaks at 1715, 1629.4, 1578,

1452.9, and 1387.7, and 1015.6 cm^{-1}, which may be attributed to the C=O stretching band, C=C stretching band for SP^2 hybridization of rGO, C–H bending of alkane, strong O–H bending of carboxylic acid groups, and strong C–O bending, respectively. Finally, in Fig. 3(A), peaks at 1636.6 and 1402.8 cm^{-1} for the NiCu powder indicate O–H bending of the Ni and Cu hydroxides. The peaks at 997.1 and 826.7 cm^{-1} are ascribed to Ni–O and Cu–O, correspondingly. In the low-frequency (800–200 cm^{-1}) area, the GO, rGO, and NiCu powders exhibit a complicated spectrum with broad bands, and they are considered as fingerprint regions.

Fig. 3(B) illustrates the FTIR charts of the NiCu/GO and NiCu/rGO nanocomposites. There are several commonalities between these two spectra with a slight difference. So, for O–H stretching, the GO and rGO nanocomposites revealed peaks at 3760.3 and 3756.3 cm^{-1}, respectively, which is greater in the case of the NiCu/GO nanocomposite due to the high OH content in the GO layers. Peaks that are near and before 3000 cm^{-1} might be ascribed to the C–H stretching of alkanes in the NiCu/GO and NiCu/rGO nanocomposites. We detected C≡C bond stretching peaks at 2367.8 and 2303 cm^{-1} as two peaks for the GO nanocomposite and one peak at 2372.8 cm^{-1} for the rGO nanocomposite, which may indicate that the C≡C bond type of the alkyne in the GO nanocomposite is completely different from the C≡C bond type of the alkyne in rGO. They are not found in the previously described GO and rGO pure samples, and their presence may also indicate the development of our bimetallic GO and rGO nanocomposites. The NiCu/rGO nanocomposite displays distinct spectral characteristics, including weak, broad, and linked peaks at particular wavenumbers. The presence of peaks at 1637.9, 1556.3, and 1464.1 cm^{-1} suggests the involvement of C=C stretching bands, which may be attributed to conjugated alkenes or the O–H bending of Ni and Cu hydroxides. These peaks also indicate the sp^2 hybridization of rGO, and the presence of C=O stretching bands or C=C stretching in cyclic alkenes. Additionally, the appearance of a peak at 1063.1 cm^{-1} is indicative of strong O–H bending in carboxylic acid groups and intense C–O bending. On the other
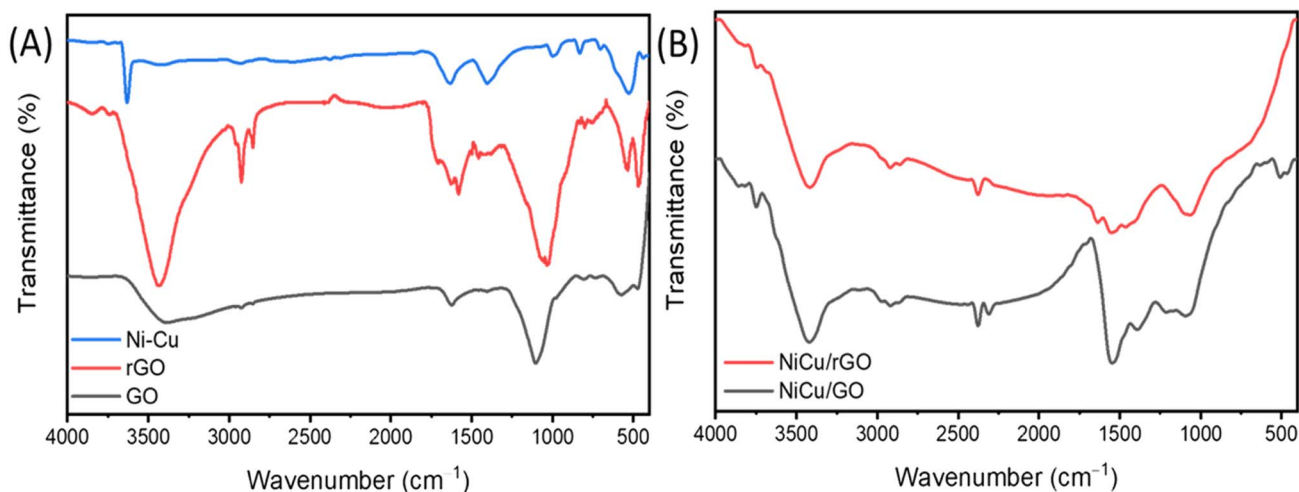

Fig. 3 FTIR of (A) GO, rGO, and NiCu samples and (B) NiCu/GO and NiCu/rGO nanocomposites.

hand, the NiCu/GO nanocomposite displays distinctive peaks at 1549.7, 1383.7, 1215.2, and 1088.7 cm^{-1}. These peaks are associated with bending modes of C=O, C=C, C–H, and O–H bonds. Furthermore, they may also arise from Ni–O and Cu–O interactions, respectively. The spectral analysis reveals important molecular characteristics of the NiCu/GO and NiCu/rGO nanocomposites, providing insights into the stretching and bending vibrations of various functional groups and chemical bonds present in the materials. In the low-frequency (800–200 cm^{-1}) area, the NiCu/GO and NiCu/rGO nanocomposites also have complex spectra with large bands, and are thought to be fingerprint areas.

In Fig. 4, the Raman study shows the peaks used to calculate the I_D/I_G band ratios of the NiCu/GO and NiCu/rGO nanocomposites, where I_D and I_G are the intensities of the defect and graphitic bands of the above-mentioned GO and rGO nanocomposites, respectively. For carbon materials, the D and G bands are mostly rather wide and overlap. The G band at 1771 cm^{-1} is associated with the stretching vibrational mode of the sp^2 hybridized carbon bonds in the graphene layer rings. The D peak at 1755 cm^{-1} is indicative of disordered carbon sp^3 regions. It is brought about by oxygen-containing groups or lattice and edge plane defects in honeycomb-like structures that both embellish and disrupt the graphitic lattice, according to Hu et al.[41] Specifically, the groups include hydroxyl (C–OH), epoxy (CO–C), carbonyl (C=O) and carboxyl (O–C=O)). These two peaks at 1755 and 1771 cm^{-1} for the two prepared nanocomposites refer to the stretching vibrational modes for the C=O and C=C bonds in the GO and rGO nanolayers. The I_D/I_G band ratios are 1.017 and 1.062 for the NiCu/GO and NiCu/rGO nanocomposites, respectively. The ratios sp^3/sp^2 and I_D/I_G are proportional. Carbon atoms that are confined by groups that contain oxygen give rise to the D band. Consequently, residual oxygen-containing groups—for instance, H$_2$O molecules vaporizing at low temperatures and oxygen-containing groups being removed at high temperatures—have an impact on the D band's intensity.[42] The increase in I_D/I_G value from 1.017 in GO

to 1.062 in the rGO composites suggests that the average size of the sp^2 dominions and the graphitic material crystallinity decreased throughout the chemical/thermal processes.

The XPS spectra that were previously reported for NiCu, NiCu/GO, and NiCu/rGO nanocomposites reveal the surface elements and groups, their binding energy, and the electronic structure of the catalysts.[43–45] For the NiCu nanocomposite, a peak at around 284 eV was attributed to the Ni^{2+} ions and the peak around 172 eV was due to the Cu^{2+} ions.[43] The peak at around 159 eV was related to the oxygen atoms, whereas the peak at around 137 eV was assigned to the carbon atoms.[43] For the NiCu/GO nanocomposite, a shift in some peaks was observed compared with that of pure NiCu. The peak at around 284 eV was shifted to higher binding energy, indicating that more oxygen atoms were present on the surface.[44] The peak at around 172 eV also was shifted slightly, suggesting that more carbon atoms were attached to the GO layer.[44] The peak at around 159 eV was unchanged, implying that there is no significant change in the oxygen content.[44] For the NiCu/rGO nanocomposite, a similar trend as that of the NiCu/GO nanocomposite was observed. However, there are some differences in some peaks.[45] For instance, the peak at around 284 eV was shifted more than that of the NiCu/GO nanocomposite, indicating that more oxygen atoms were present on both sides of the rGO layer.[45] The peak at around 172 eV also shifted more than that of the NiCu/GO nanocomposite, suggesting that more carbon atoms were attached to both sides of the rGO layer.[45] The peak at around 159 eV was unchanged, implying that there was no significant change in the oxygen content.[45] These studies showed that adding GO or rGO as support enhances both the number and distribution of active sites for the Ni–Cu bimetallic catalysts. This may improve their catalytic performance for DAFCs by increasing their stability and activity.

3.1.3. Optical absorption. A UV-Vis spectrophotometer was used to study the optical absorption and bandgap of the NiCu, rGO, NiCu/rGO, and NiCu/GO nanocomposites. Fig. 5(a) and (b) illustrates the absorption spectra in the 200–800 nm range at AT. The absorption decreases noticeably with increasing wavelength. Two absorption peaks were observed in the UV-visible spectrum of the rGO nanomaterials, as presented in Fig. 5(a) rGO showed a strong band at 260 nm and a small shoulder at 375 nm. The strong band for rGO at 260 nm is assigned to the π–π* transitions. The small peak at 375 nm is related to the n–π* transitions. For the NiCu spectrum, the strong visible light absorption intensities are caused by the strong electronic transition from the valence (2p O^{-2}) to conduction (3d/4s metallic ion orbitals) bands.[46] For the NiCu/rGO composite (Fig. 5(b)), small absorption peaks are observed at 267 and 357 nm. This is quite similar to data presented by Abid et al.,[47] where an absorption peak at 266 nm was observed for rGO.

The optical band gap for the direct allowed transitions of the synthesized nanocomposites was estimated utilizing Tauc's formula (eqn (1)).
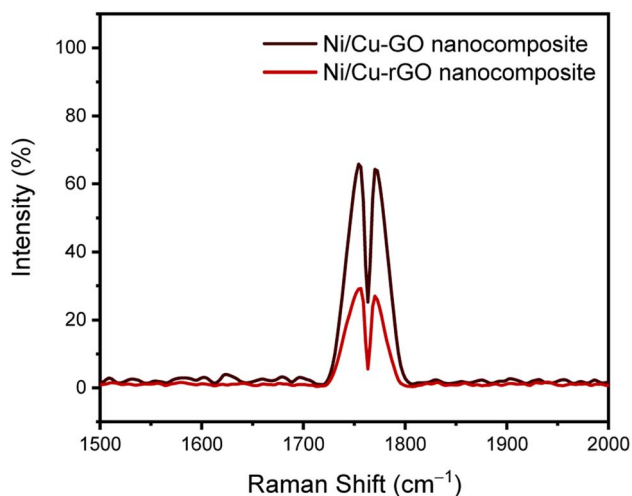
Fig. 4 Raman charts of the NiCu/GO and NiCu/rGO nanocomposites.

$$\alpha = \left(E - E_g\right)^{\frac{1}{2}} \Big/ h\nu \qquad (1)$$
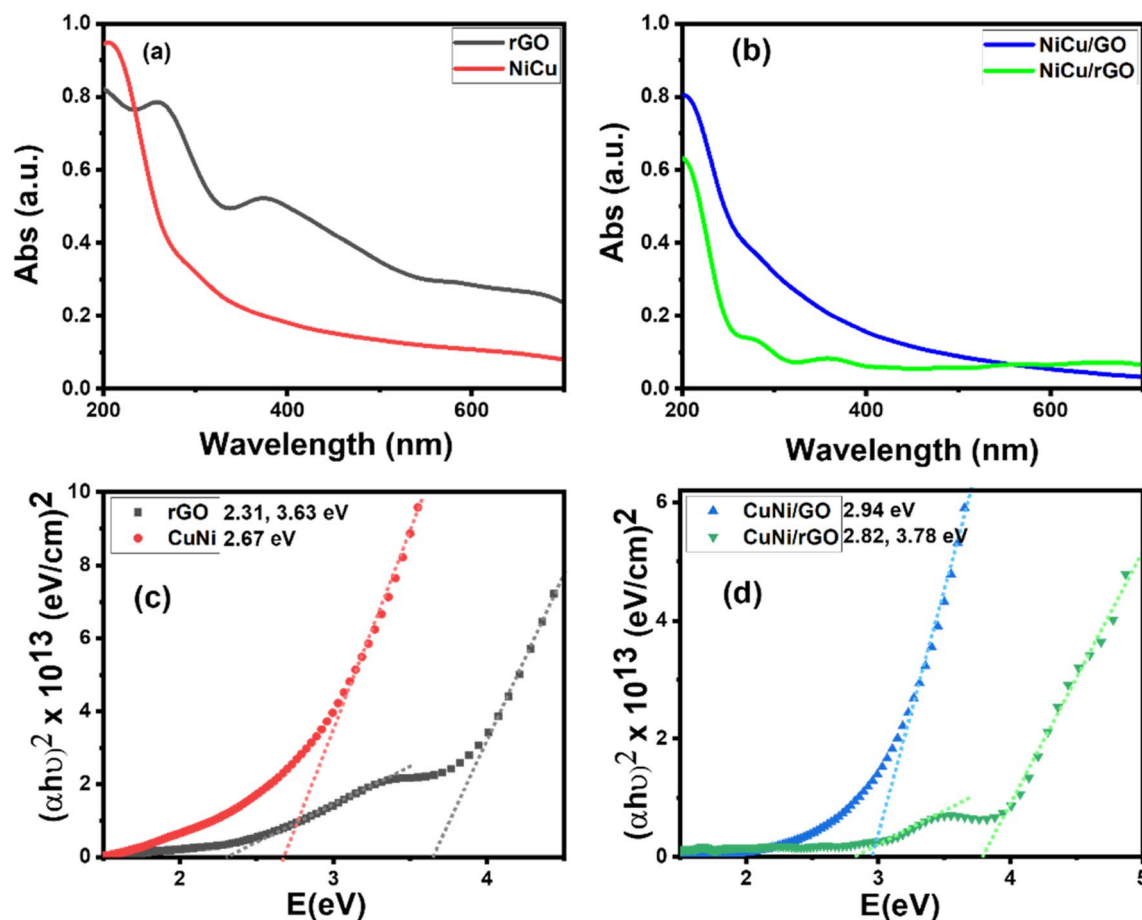
Fig. 5 (a) and (b) UV-vis absorption spectra and (c) and (d) Tauc plots for the samples rGO, NiCu, NiCu/GO, and NiCu/rGO.

where α, E, and E_g are the optical absorption coefficient (cm^{-1}), photon energy (eV), and direct bandgap (eV), respectively.[48] h and ν represent Planck's constant (J s) and the frequency of the incident photons (Hz), respectively. α was calculated by eqn (2);

$$\alpha = 2.303 \times 10^3 A\beta/lC \qquad (2)$$

where A is the sample's absorbance, β is the material's density (g cm^{-3}), l is the optical path (1 cm), and C is the amount of nanocomposite in the suspension (g). Fig. 5(c) and (d) shows plots between $(\alpha h\nu)^2$ and E for the examined samples. The straight-line portions of the curves were used to obtain the bandgap values. In contrast to rGO, which exhibited optical band gaps of 2.31 and 3.63 eV, the NiCu composite had an optical band gap of 2.67 eV. The band gap is decreased from 2.94 to 2.82 eV by employing rGO as a host for NiCu instead of GO, as illustrated in Fig. 5(d). This decrease may be caused by rGO's functional groups that include oxygen, which can cause the optical band gap to become narrow.[49] In nanomaterials with a narrower bandgap, the electrons can move from the VB to the CB more easily. This suggests increased electrical conductivity and electron concentration for NiCu/rGO.[50]

3.1.4. Structural properties. The crystal structure of the nanocomposites NiCu, NiCu/GO, and NiCu/rGO is shown by the XRD patterns in Fig. 6. The hydrothermal process transforms

the additives into a mixture of nano-sized $Ni(OH)_2$ and CuO.[51,52] The peaks at 2θ = 19.1°(001), 38.7°(011), and 52.2°(012) confirmed the formation of the β-$Ni(OH)_2$ phase (JCPDS, file No. 14-0117).[53] The diffraction peaks at 2θ values of 35.4°(002), 38.8°(200), 48.7°(−202), 61.5°(−113), 66.4°(022), and 68.1°(220) correspond to monoclinic CuO with the $C2/c$ space group (JCPDS file No. 45-937).[54] The other detected peaks are related to α-$Ni(OH)_2$ with a major peak at 35.4°, which is compatible with literature values (JCPDS 41-1424).[55,56] The samples have a pure phase structure, as no impurity peaks from KOH, $NiCl_2$, or $CuCl_2$ are detected.

In Fig. 6(B), the diffraction peaks at 2θ of 19.4, 25.7, 36.5, 38.7, 42.5, 43.6, 52.5, 59.4, 61.7, 73.6, and 74.4° are observed. The intense and narrow diffraction peak at 2θ = 36.5° suggests an increase in the crystallinity of $Ni(OH)_2$/CuO on the GO nanosheets. The GO nanosheets may be represented by the broad peaks at 19.4 and 25.7.[57] In Fig. 6(C), these peaks merge into one peak at 24.9°, which is attributed to the reduction of the GO nanosheets. The shift of the characteristic peak from 19.4° to 24.9° after simultaneous hydrothermal treatment at 200 °C and chemical reduction using hydrazine indicates that GO is fully reduced to rGO in the NiCu/rGO nanocomposite.[58]

The Debye–Scherrer equation (eqn (3)) can be used to calculate the crystallite size, D (nm), from the diffraction angle,
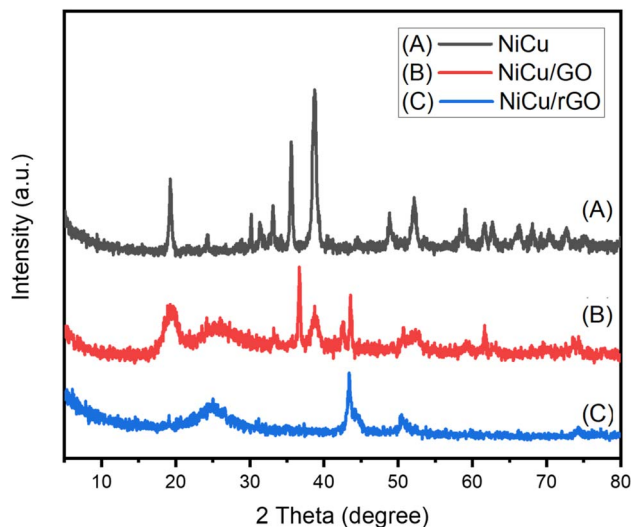
Fig. 6 XRD patterns of (A) NiCu, (B) NiCu/GO, and (C) NiCu/rGO nanocomposites.

θ (degree), the X-ray wavelength, λ (=0.154 nm), and the full width at half maximum, β (rad):[57,59]

$$D = 0.98\lambda/\beta \cos\theta \qquad (3)$$

The values of the average crystallite size are 27.8, 21.7, and 8.9 nm for NiCu, NiCu/GO, and NiCu/rGO, respectively. The reduction of the crystallite size, by loading NiCu on the surface of rGO and GO, refers to the enhancement of the specific surface area (SSA, area per unit mass). The minimum dislocation density, $1/D^2$, is calculated to be 1.88×10^{-3}, 18.59×10^{-3}, and 31.4×10^{-3} dislocation per nm^2 for NiCu, NiCu/GO, and NiCu/rGO, respectively.[60] The SSA of the samples is an important structural parameter. The values of this parameter are calculated by SSA = $6000/(D \times \rho)$, where ρ is the density of nanoparticles.[58,61] The ratios of SSA for CuNi/rGO and CuNi/GO relative to NiCu are calculated to be 4.04 and 1.87, respectively.

Therefore, the NiCu/rGO nanocomposite is supposed to be more catalytically effective than pure NiCu.

3.2. Electrochemical oxidation (ECO)

3.2.1. Impact of electrolytes and samples compositions. The electrocatalytic activity for the oxidization of 0.5 M ethanol and 2 M methanol in 1 M KOH solution at AT and 100 mV s^{-1} scanning rate is affected by the compositions of the samples, as illustrated in Fig. 7. 0.5 M for ethanol and 2 M for methanol were chosen by optimizing their concentrations, as shown in Fig. 7. In 0.5 M ethanol (Fig. 7(A)), when rGO is added to the NiCu nanocomposite, the maximum current density rises from 0.096 to 0.244 A g^{-1}, showing an enhancement in the electrocatalytic performance. However, the addition of graphene oxide slightly increased the current density from 0.096 to 0.101 A g^{-1}. In 2 M methanol (Fig. 7(B)), by employing GO and rGO as supports, respectively, the maximum current density of the NiCu nanocomposite is increased from 0.08 to 0.11 and 0.267 A g^{-1}, significantly boosting the electrocatalytic performance. By adding GO, the oxidation peak's current density is raised from 0.039 A g^{-1} at 0.63 V to 0.105 A g^{-1} at 0.79 V. Conversely, the incorporation of rGO increases its current density to 0.212 A g^{-1} @ 0.83 V, i.e., the NiCu-rGO nanocomposite gives a higher oxidation current density than the other catalysts and the enhancement reached 468.2% compared to the pure NiCu composite. This enhancement is associated with an increase in electric conductivity, mobility, and surface area, which increases throughout the rGO reduction procedure.[62] Similarly, Noor et al.[31] and Al-Enizi et al.[63] found comparable characteristics for rGO-MOFs nanocomposites, albeit with lesser enhancements than this study.

The electrochemical oxidation of methanol and ethanol is a process that involves the transfer of electrons from these alcohols to an electrode, usually made of a metal catalyst. The adsorption mechanism is the way that the alcohol molecules interact with the surface of the catalyst, which affects the rate and selectivity of the reaction. Adsorption can be classified into
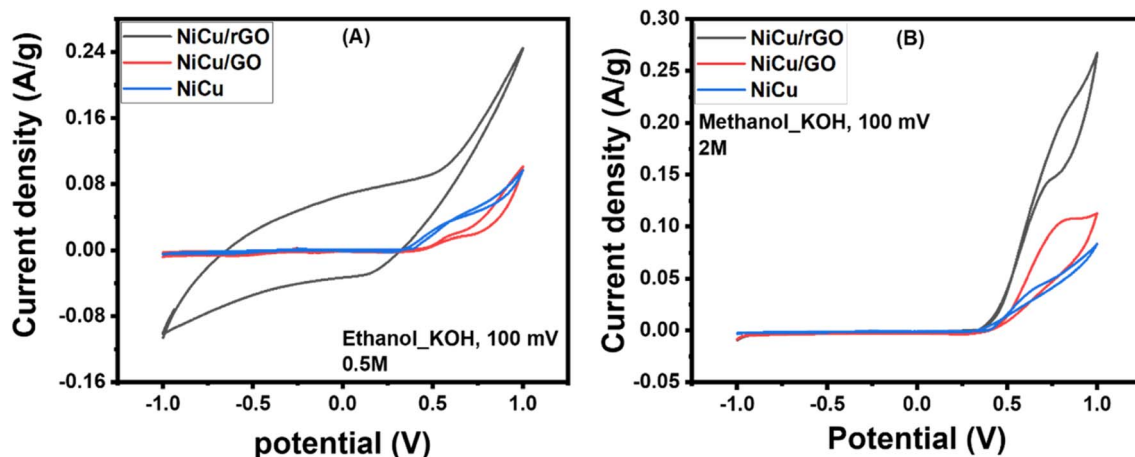

Fig. 7 The impact of the sample compositions on electrocatalytic performance using 1 M KOH solutions at 20 °C to oxidize (A) 0.5 M ethanol and (B) 2 M methanol.

two types: physisorption and chemisorption. Physisorption uses weak van der Waals forces, whereas chemisorption uses strong covalent bonds.[64] The adsorption energy indicates how strongly the adsorbate binds to the adsorbent surface, *i.e.*, the adsorption energy is the amount of energy released or consumed when the alcohol molecules bind to the catalyst surface, which reflects the strength and stability of the adsorption. It is computed by subtracting the total energy of the system before adsorption from the total energy after adsorption.[65] Previous studies have demonstrated that NiCu bimetallic alloys are effective catalysts for methanol and ethanol oxidation. This is because of the cooperative effects of the Ni and Cu atoms and the favorable hydrogen adsorption energy of NiCu.[22,66] NiCu/GO and NiCu/rGO are hybrid materials that integrate the benefits of NiCu alloys and graphene oxide (GO) or reduced graphene oxide (rGO) as supports. GO and rGO can enhance the distribution and stability of NiCu nanoparticles, and also offer high electrical conductivity and large surface area.[66] The adsorption processes of NiCu, NiCu/GO, and NiCu/rGO for methanol and ethanol oxidation are complicated and influenced by the surface structure, composition, and morphology of the catalysts, as well as the reaction conditions. Some potential steps that are involved include the following: (a) adsorption of methanol or ethanol molecules on the catalyst surface, (b) dehydrogenation of methanol or ethanol to produce CO and H_2,

(c) oxidation of CO to CO_2, and (d) desorption of CO_2 and H_2O from the catalyst surface.[22,66]

3.2.2. Impact of electrolyte concentrations. Ni-based electrodes are considered the most effective electrocatalyst for oxidizing ethanol and methanol.[67] The obtained nanocomposites' CV curves at various ethanol and methanol concentrations are shown in Fig. 8. The adsorption of the reactants and intermediate components, followed by dissociation phases, is the basis of the ethanol ECO processes to determine the selectivity and efficiency of the reaction.[68] Hence, it is important to optimize the ethanol concentration. For the NiCu/rGO nanocomposite as shown in Fig. 8(A), when the ethanol concentration decreased from 2 M to 0.5 M, the maximum current density rose from 0.096 to 0.246 A g^{-1}. This suggests that the NiCu/rGO nanocatalyst exhibits its best EC catalytic activity at 0.5 M ethanol concentration. Because ethanol covers more hot spots with increasing concentrations, hydroxyl is unable to bind to the active sites.[69]

The concentration was also optimized for the ECO of methanol using the NiCu/rGO nanocatalyst (Fig. 8(B)). The maximum current density for methanol increased from 0.207 to 0.266 A g^{-1} as the methanol concentration climbed from 0.5 M to 2 M. The current densities of the oxidation peaks changed from 0.10 A g^{-1} @ 0.711 V to 0.20 A g^{-1} @ 0.807 V as the methanol concentration changed from 0.5 M to 2 M, *i.e.*, the

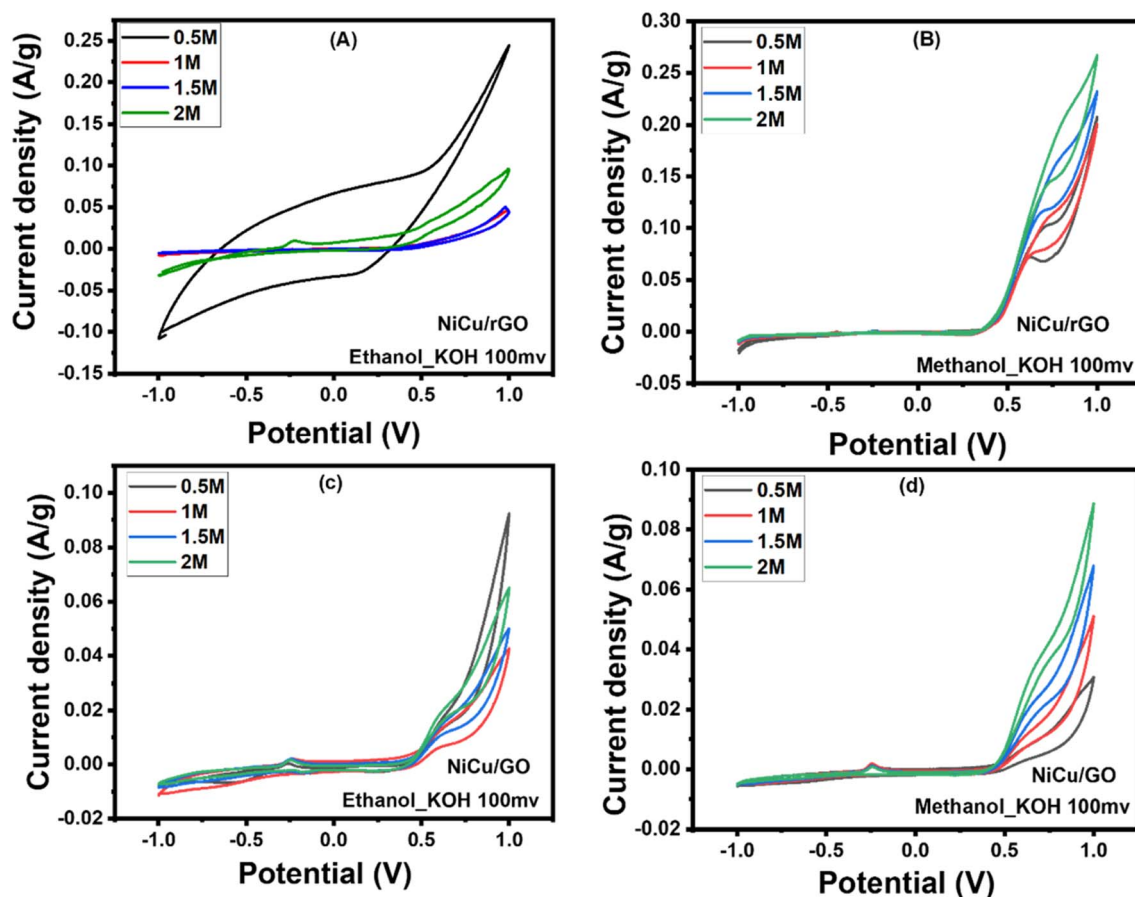
Fig. 8 Effects of ethanol and methanol concentrations on the EC catalytic activity of NiCu/rGO (A) and (B) and NiCu/GO (C) and (D) at AT.
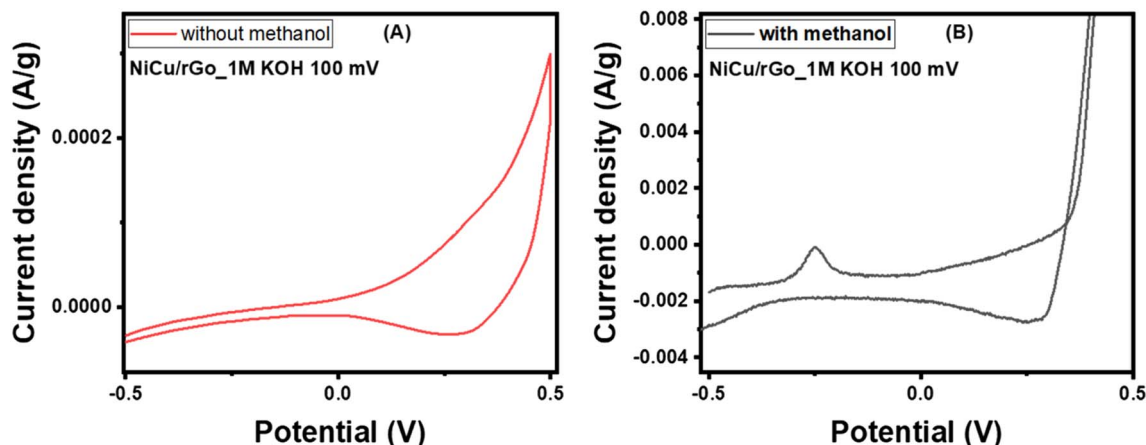
© 2024 The Author(s). Published by the Royal Society of Chemistry

Fig. 9 CV plots at a scanning rate of 100 mV s^{-1} for NiCu/rGO in 1 M KOH (A) without methanol and (B) with methanol.

ideal methanol concentration for the NiCu/rGO nanocomposite is 2 M.

For the NiCu/GO nanocomposite (Fig. 8(C) and (D)), the optimum concentrations of 0.5 M ethanol and 2 M methanol had the highest current density values of 0.09 and 0.08 A g^{-1}, respectively. Also, the highest values for the oxidation peak are 0.002 A g^{-1} @ 0.24 V for 0.5 M ethanol and 0.001 A g^{-1} @ 0.24 V for 2 M methanol. Therefore, these values indicate that the prepared nanocomposites are more efficient for the electro-oxidation of methanol than ethanol. Hence, a high methanol concentration may inhibit the catalyst's ability to oxidize,

leaving the oxygen evolution reaction (OER) active site unoccupied and reducing the competitive connection between the OER and the methanol ECO process.[46] Similar results are observed by Deng *et al.*[70] using the NiCo/C–N/CNT electrocatalyst, which is a more complicated structure.

The impact of 1 M KOH electrolyte with and without methanol on the ECO process is depicted in Fig. 9. The presence of the oxidation peak of NiCu/rGo in the CV curve obtained in the 1 M KOH + 2.0 M methanol electrolyte indicates the occurrence of catalyst electrooxidation due to the breakdown of the electronic bonds and the production of oxyhydroxide (OOH).[71]
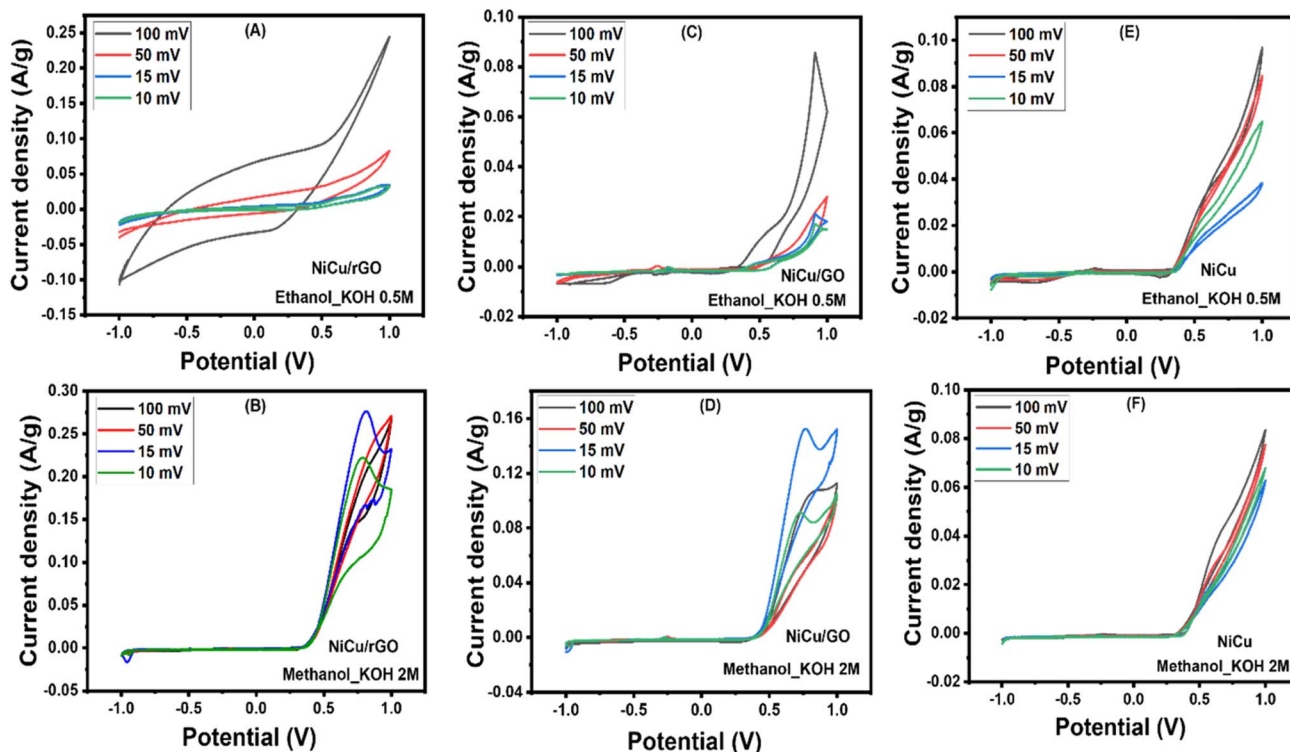

Fig. 10 Scanning rate effect on the EC catalytic performance of (A) and (B) NiCu/rGO, (C) and (D) NiCu/GO, and (E) and (F) NiCu for ethanol and methanol ECO at AT.

RSC Advances

Paper

3.2.3. Scanning rate effect. The catalytic performance of NiCu/rGO, NiCu/GO, and NiCu for ECO of ethanol and methanol in 1 M KOH electrolyte at AT is shown *versus* the scanning rate in Fig. 9. The current densities for all samples in 0.5 M ethanol, as well as NiCu in 2.0 M methanol, rose as the scanning rate rose to 100 mV, as illustrated in Fig. 10(A), (C), (E), and (F).[72] The rate of diffusion outpaces the response rate at higher scan rates. As a result, additional electrolytic ions arrive at the electrode–electrolyte interfaces, but fewer ions take part in the charge transfer process. Then, the optimal scanning rate is 100 mV s^{-1}.[73] The optimal scan rate, however, changes to 10 mV when GO and rGO are added to the composite at 2 M methanol (Fig. 10(B) and (D)). This could be true given that the electrode's external surface experiences the greatest amount of electrolytic ion intercalation at the slowest scanning rate.[74]

3.2.4. LSV measurements. Fig. 11(A)–(C) illustrates the LSV plots using NiCu/rGO, NiCu/GO, and NiCu in ethanol and methanol at the optimum concentrations utilizing the three-electrode cells. The scanned potential window ranges from −1 to +1 V at 100 mV s^{-1}. For NiCu/rGO (Fig. 11(A)), the current densities changed from 0.094 to 0.326 A g^{-1} for ethanol and methanol, respectively. For NiCu/GO, Fig. 10(B), the current density increased from 0.125 to 0.266 A g^{-1} for ethanol and methanol, respectively. For NiCu, Fig. 10(C), it is changed from 0.046 to 0.07 A g^{-1} for ethanol and methanol, respectively.

These values clearly indicate the enhancement that happened due to the loading of NiCu on rGO and GO. GO and rGO have large surface areas and high electrical conductivities. Therefore, the loading of the Cu/Ni composite on GO and rGO can enhance the electrochemical oxidation performance of methanol and ethanol by providing more active sites, improving the electron transfer, increasing stability, enhancing mass transport, and creating a synergistic effect.[75] The activities of the materials under examination can also be detected using the onset potentials (E_{onset}).[76] The E_{onset} of NiCu, NiCu/GO, NiCu/rGO is 377 mV, −279 mV and −509 mV, respectively. In comparison to all samples, the electrocatalytic activity and onset potential data show that NiCu/rGO is a more potent catalyst for the methanol ECO. When using the NiCu/rGO composite, the higher ECO current density of methanol compared to ethanol can be attributed to its simpler molecular structure, weaker bonding energy, stronger adsorption properties, higher surface coverage, and better mass transport properties.[77]

3.2.5. Chronoamperometric (CAM) measurements. The CAM measurements are used to evaluate the catalytic stabilities of the electrodes. The stability of NiCu/rGO and NiCu/GO was assessed for a long duration, and is presented in Fig. 11(D). A long-period CAM test was also carried out for 300 min and provided as ESI (Fig. S1†). NiCu/rGO demonstrated greater stability during the methanol ECO process as compared to
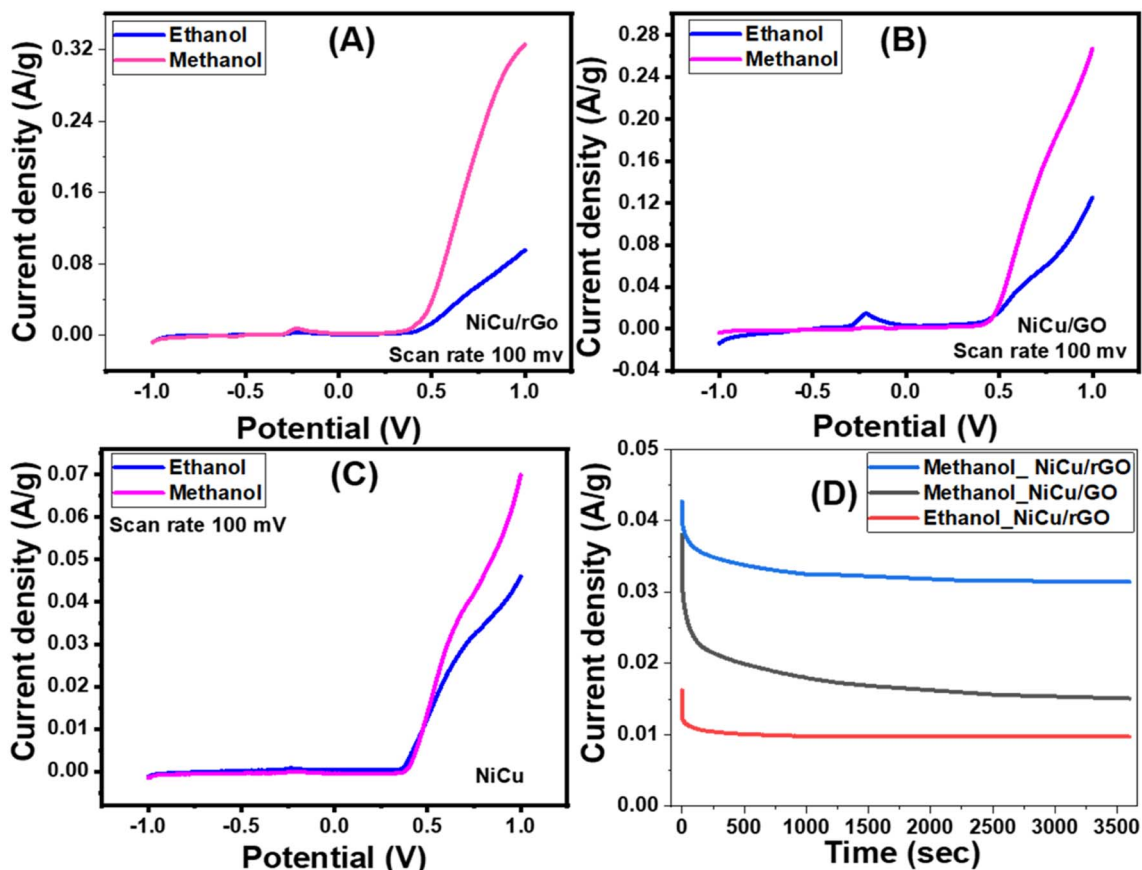

Fig. 11 Linear sweep voltammetry plots at 100 mV s^{-1} for (A) NiCu/rGO, (B) NiCu/GO, and (C) NiCu. (D) The variation of the current density *versus* time, CAM measurements, in ethanol and methanol at optimized concentrations.

ethanol ECO with current densities of 0.0315 and 0.0098 A g⁻¹, respectively. The starting fast reduction before reaching a constant output rate is caused by a small corrosion activity across the electrode-redox electrolyte interface.[78] NiCu/GO showed a lower stable current (0.0155 A g⁻¹) for the methanol electrooxidation than the NiCu/rGO electrode. This indicates that, despite the initial decrease in the density of currents, the NiCu/rGO electrode showed high chemical stability and an extended lifespan as a functional ECO electrode, as shown in Fig. S2.†

3.2.6. EC impedance (ECI) spectroscopy. The charge carriers' dynamics play a major role in determining the electrooxidation's catalytic performance for the used electrodes. The CHI EC station was used to measure the ECI data at AT to characterize the interfacial properties of the electrocatalysts.[78]

Table 2 Randle circuit values estimated from ECI data for the studied electrodes

Catalyst	R_s/Ω	R_{ct}/Ω	$C_{dl}/\mu F$	Z_W	$\theta_{max}/degree$	f_{max}/Hz	τ_n/ms
CuNi/rGO	36.4	7.5	3.53	1.34	72.0	33.85	29.5
					69.4	1.40	714.3
CuNi/GO	37.2	1.2	2.09	1.57	78.36	2.59	386.1
CuNi	35.4	3.34	0.78	6.36	81.84°	13.40	74.6

Impedance is the sum of the real and imaginary (Z', Z'') elements of the cell's resistance and capacitance, respectively.[79] ECI analyses were carried out from 0.1 to 100 000 Hz, with the electrodes dipped in 2 M methanol electrolyte and illuminated. The Nyquist graphs for the electrodes are displayed in
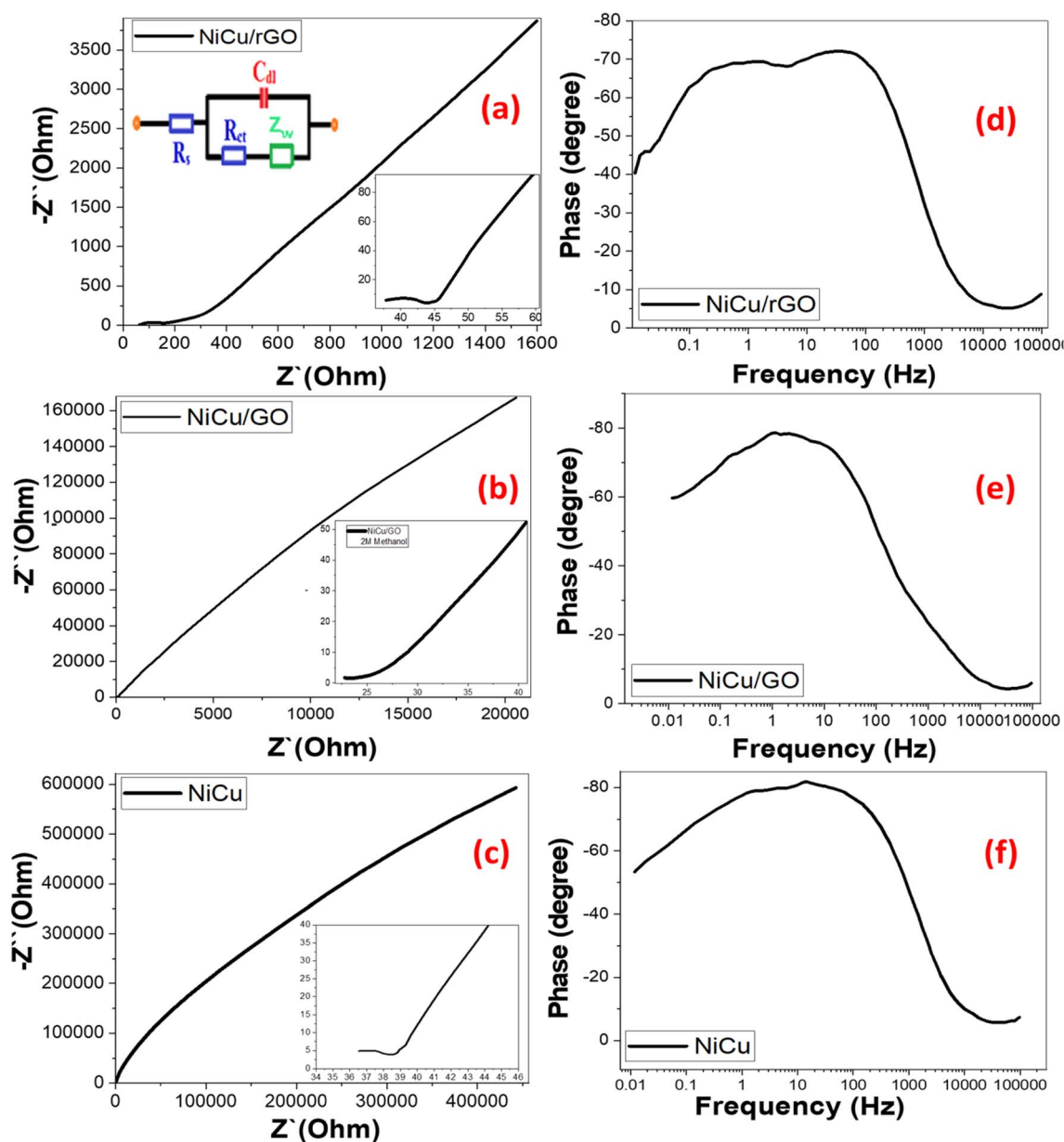

Fig. 12 Nyquist and Bode plots for electrodes NiCu/rGO (A) and (D), NiCu/GO (B) and (E), and NiCu (C) and (F) in 2 M methanol.

Table 3 Comparison of the designed NiCu/rGO and NiCu/GO electrocatalysts with the previously reported Pt-based or Ni-based electro-catalysts for DAFC application

Catalyst	Morphology	Electrolyte	E_{Onset} (mv)	Current density	Catalyst dose	Ref.
$Pt_{79}Fe_{21}$/N-doped graphene	Alloy nanoparticles/ sheets	0.5 M H_2SO_4 + 1 M HCOOH	110 mV vs. RHE	186 mA g^{-1} at 400 mV vs. RHE	2 mg	83
Pt_1Ru_2/microporous carbon-950	Alloy nanoparticles/ microporous	0.5 M H_2SO_4 + 1 M CH_2O_2	110 mV vs. Ag/ AgCl	9.5 mA cm^{-2} at 0.70 V	10 mg	84
PtAu-on-Au	Nanostructure	0.5 M HCOOH + 0.5 M H_2SO_4	—	228 mA g^{-1} @ 0.51 V	8 mg	85
Pd_2Ni_3/C	Nanopowder	1 M ethanol + 1 M KOH	−0.65 V vs. MMO	217 mA cm^{-2}	10 mg	86
$NiCo_2S_4$/CNT (3 : 1)	Nanocomposite	1 M methanol + 1 M KOH	—	160 mA cm^{-2} at 0.6 V	4 mg	87
Pd@PdPt	Porous core/shell nanocubes	0.5 M KOH + 1 M ethanol	0.467 V vs. RHE	3.449 mA cm^{-2}	—	88
PdPt/C	Nanoparticles	0.3 M KOH + 1 M ethanol	−0.37 V	3.27 mA cm^{-2}	1 mg	89
$Pt_1Ru_{0.5}Sn_{0.5}$-RGO	Alloy nanoparticles	1 M KOH + 1 M ethanol	−0.633 V	2.489 mA cm^{-2}	3 mg	90
Rh@Pt	Core–shell nanocubes	0.2 M ethanol + 0.1 M $HClO_4$	0.46 V vs. RHE	2.62 mA cm^{-2}	—	91
PtCoRh	Nanoassemblies	1 M KOH + 1 M ethanol	0.25 V vs. RHE	40.3 mA cm^{-2}	2 mg	92
NiCu/rGO	Nanospheres on nanosheets	1 M KOH + 2 M methanol	−509 vs. Hg/ HgCl	267 mA g^{-1}	25 mg	This study

Fig. 12(a)–(c). The corresponding Bode plots are shown in Fig. 12(d)–(f). All working electrodes showed a very low electrode/electrolyte charge transfer resistance (R_{ct}, small semicircle) at high frequencies.[80] At low frequencies, straight line segments are observed because of diffusion-controlled routes (Warburg impedance, Z_w) and double-layer capacitance (C_{dl}). The data are simulated and fitted using Randall's comparable circuit consisting of active electrolyte resistance (R_S), R_{ct}, Z_w, and C_{dl}. The values of the elements are reported in Table 2. The value of Z_w is reduced by loading NiCu on the GO and rGO surfaces, indicating improved performance by adding rGO. All samples had low R_{ct}, which indicates reduced charge recombinations at the electrode/electrolyte interfaces.[81] The highest phase shift (θ_{max}) and the frequency (f_{max}) at θ_{max} are determined from Fig. 12(d)–(f) for NiCu/rGO, NiCu/GO and NiCu, and summarized in Table 2. Similar to the observed optical behavior, NiCu/rGO had two maxima while Ni/Cu/GO displayed just one maximum.

The values of f_{max} are used to predict the charge carriers' lifetimes, as shown in Table 2.[82] Much higher values of the charge carrier lifetime are observed by loading NiCu on rGO and GO. This also confirms that the addition of rGO significantly reduces the charges recombinations through the electrode/ electrolyte interface. This also involves kinetically straightforward electrooxidation processes, electrolyte diffusion, and improved ionic conductivity through the NiCu/rGO electrode. Hence, NiCu/rGO and NiCu/GO exhibited superior electro-oxidation catalytic performance compared to the NiCu electrode.

Table 3 shows a comparison between the performance of our optimized catalysts (NiCu/rGO) and the previously reported Pt-based or Ni-based catalysts that are used for the electro-oxidation of methanol or ethanol.[83–92] The designed NiCu/rGO catalyst exhibits a higher current density and a lower onset potential than most of the reported Pt-based or Ni-based electrocatalysts for DAFC application, demonstrating better electrooxidation catalytic activity. The designed NiCu/rGO catalyst has a similar morphology to some of the reported electrocatalysts but with different compositions and electrolytes, and a higher catalyst dose, which may affect its cost-effectiveness and stability. Hence, the properties of the bimetallic NiCu/ rGO suggest that it could potentially serve as a less expensive alternative to high-priced DAFC catalysts. Ding et al.[93] and Zhao et al.[94] have proposed a novel approach that uses ML to design and optimize PEMFCs. ML can analyze large and complex datasets, either experimental or theoretical, and predict the output with fewer trials.[93,94] Our future work will use ML to optimize the catalysts' synthesis, performance, and cost, and to understand their mechanisms and interactions with the fuel and the membrane. We will also validate the catalysts in real DAFC systems, compare them with Pt-based catalysts, and explore other metal alloys and graphene derivatives as potential electrocatalysts for DAFCs.

4. Conclusion

A one-step hydrothermal method is successfully adapted for the *in situ* design of NiCu and its composites, NiCu/GO and NiCu/ rGO. The sample morphologies, chemical compositions and functional groups, and optical band gaps were studied using SEM, EDX, FTIR, Raman, and UV/Vis spectroscopy. NiCu/rGO demonstrated the best electrochemical activity of all

synthesized catalysts, having 267 mA g^{-1} current density and the lowest onset potential and impedance due to rGO, which caused agglomeration. The performance of NiCu is improved by 468.2% and 377.7% in methanol and 255.6% and 105.9% in ethanol, respectively, when rGO and GO are used as supports. Also, the working NiCu/rGO electrode for the electrooxidation showed the highest chemical stability, longest lifetime, lowest Warburg impedance, and longest charge carriers' lifetime. The characteristics of this bimetallic NiCu/rGO make it a possible replacement for the costly DAFC catalysts.

Author contributions

Conceptualization, A. M., M. G. M. K., and M. S.; methodology, A. M., M. G. M. K., and M. S.; validation, A. M., H. H., M. F. E. and M. S.; formal analysis, A. M., M. F. E., M. G. M. K., and M. S.; investigation, A. M., M. G. M. K., G. M. A., and M. S.; resources, A. M., G. M. A., and M. S.; data curation, A. M., M. G. M. K., G. M. A., and M. S.; writing—original draft preparation, A. M., M. G. M. K., and M. S.; writing—review and editing, A. M., M. G. M. K., M. F. E., G. M. A., H. H., and M. S.; visualization, A. M., H. H., M. G. M. K., M. F. E., G. M. A., and M. S.; project administration G. M. A., M. S., and H. H.; funding acquisition, G. M. A. and M. S. All authors have read and agreed to the published version of the manuscript.

Conflicts of interest

The authors declare no conflict of interest.

Acknowledgements

References

1 R. Lei, S. Feng and T. Lauvaux, Country-Scale Trends in Air Pollution and Fossil Fuel CO2 Emissions during 2001–2018: Confronting the Roles of National Policies and Economic Growth, *Environ. Res. Lett.*, 2020, **16**, 014006.

2 A. B. Stambouli and E. Traversa, Solid Oxide Fuel Cells (SOFCs): A Review of an Environmentally Clean and Efficient Source of Energy, *Renewable Sustainable Energy Rev.*, 2002, **6**, 433–455.

3 S. Mekhilef, R. Saidur and A. Safari, Comparative Study of Different Fuel Cell Technologies, *Renewable Sustainable Energy Rev.*, 2012, **16**, 981–989.

4 C. Lamy, A. Lima, V. LeRhun, F. Delime, C. Coutanceau and J.-M. Léger, Recent Advances in the Development of Direct Alcohol Fuel Cells (DAFC), *J. Power Sources*, 2002, **105**, 283–296.

5 J. Wang, X. Cao, L. Fang, X. You, K. Wong, S. Cao, C. Xiao, S. Cai, Y. Huang and X. Zhang, MoS2 Nanoflower Supported Pt Nanoparticle as an Efficient Electrocatalyst for Ethanol Oxidation Reaction, *Int. J. Hydrogen Energy*, 2019, **44**, 16411–16423.

6 T. Iwasita, R. Dalbeck, E. Pastor and X. Xia, Progress in the Study of Electrocatalytic Reactions of Organic Species, *Electrochim. Acta*, 1994, **39**, 1817–1823.

7 L. T. Tran, Q. M. Nguyen, M. D. Nguyen, H. N. T. Le, T. T. Nguyen and T. H. T. Vu, Preparation and Electrocatalytic Characteristics of the Pt-Based Anode Catalysts for Ethanol Oxidation in Acid and Alkaline Media, *Int. J. Hydrogen Energy*, 2018, **43**, 20563–20572.

8 H. Zhang, M. Jin, H. Liu, J. Wang, M. J. Kim, D. Yang, Z. Xie, J. Liu and Y. Xia, Facile Synthesis of Pd–Pt Alloy Nanocages and Their Enhanced Performance for Preferential Oxidation of CO in Excess Hydrogen, *ACS Nano*, 2011, **5**, 8212–8222.

9 A. Hajian, A. A. Rafati, O. Yurchenko, G. Urban, A. Afraz, M. Najafi and A. Bagheri, Nanostructured Flower like Pt-Ru for Ethanol Oxidation and Determination, *J. Electrochem. Soc.*, 2014, **162**, B41.

10 D. Pakhare and J. Spivey, A Review of Dry (CO 2) Reforming of Methane over Noble Metal Catalysts, *Chem. Soc. Rev.*, 2014, **43**, 7813–7837.

11 M. Li, B. Hua, J. Luo, J. Pu, B. Chi and L. Jian, Carbon-Tolerant Ni-Based Cermet Anodes Modified by Proton Conducting Yttrium-and Ytterbium-Doped Barium Cerates for Direct Methane Solid Oxide Fuel Cells, *J. Mater. Chem. A*, 2015, **3**, 21609–21617.

12 X. Luo, J. Wang, M. Dooner and J. Clarke, Overview of Current Development in Electrical Energy Storage Technologies and the Application Potential in Power System Operation, *Appl. Energy*, 2015, **137**, 511–536.

13 I. Danaee, M. Jafarian, F. Forouzandeh, F. Gobal and M. G. Mahjani, Electrocatalytic Oxidation of Methanol on Ni and NiCu Alloy Modified Glassy Carbon Electrode, *Int. J. Hydrogen Energy*, 2008, **33**, 4367–4376.

14 M. Sundaram, A. B. Kamaraj and G. Lillie, Experimental Study of Localized Electrochemical Deposition of Ni-Cu Alloy Using a Moving Anode, *Procedia CIRP*, 2018, **68**, 227–231.

15 R. Casati and M. Vedani, Metal Matrix Composites Reinforced by Nano-Particles—a Review, *Metals*, 2014, **4**, 65–83.

16 A. Naseer, F. Ahmad, M. Aslam, B. H. Guan, W. S. W. Harun, N. Muhamad, M. R. Raza and R. M. German, A Review of Processing Techniques for Graphene-Reinforced Metal Matrix Composites, *Mater. Manuf. Processes*, 2019, **34**, 957–985.

17 C. Lee, X. Wei, J. W. Kysar and J. Hone, Measurement of the Elastic Properties and Intrinsic Strength of Monolayer Graphene, *Science*, 2008, **321**, 385–388.

18 T. Kuilla, S. Bhadra, D. Yao, N. H. Kim, S. Bose and J. H. Lee, Recent Advances in Graphene Based Polymer Composites, *Prog. Polym. Sci.*, 2010, **35**, 1350–1375.

19 Y. Cui, S. I. Kundalwal and S. Kumar, Gas Barrier Performance of Graphene/Polymer Nanocomposites, *Carbon*, 2016, **98**, 313–333.

20 M. Wala, M. Szewczyk, K. Leśniak-Ziółkowska, A. Kazek-Kęsik and W. Simka, Preparation of NiCuGO Composite and Investigation of Its Electrocatalytic Properties in Methanol Oxidation, *Electrochim. Acta*, 2022, **425**, 140743.

21 M. Wala, A. Blacha-Grzechnik, A. Stolarczyk, S. Bajkacz, P. Dydo and W. Simka, Unexpected Electrochemical Oxidation of Urea on a New NiCuGO Composite Catalyst, *Int. J. Hydrogen Energy*, 2023, **48**(88), 34229–34243.

22 B. M. Thamer, M. M. A. Hameed, H. S. Abdo and M. H. El-Newehy, Bimetallic NiCu Alloy Nanoparticles Supported on Porous Carbon Nanosheets as an Efficient Electrocatalyst for Methanol and Urea Electrooxidation, *Ionics*, 2023, **29**, 4203–4215.

23 S. Gupta and M. De, Role of Metal (Cu/Ni/Fe/Co)-Carbon Composite in Enhancing Electro-Oxidation of Ethylene Glycol, *J. Appl. Electrochem.*, 2023, 1–15.

24 N. M. S. Hidayah, W.-W. Liu, C.-W. Lai, N. Z. Noriman, C.-S. Khe; U. Hashim and H. C. Lee, Comparison on Graphite, Graphene Oxide and Reduced Graphene Oxide: Synthesis and Characterization, In *Proceedings of the AIP conference proceedings*, AIP Publishing, 2017, vol. 1892.

25 A. Pareek, J. S. Sravan and S. V. Mohan, Exploring Chemically Reduced Graphene Oxide Electrode for Power Generation in Microbial Fuel Cell, *Mater. Sci. Energy Technol.*, 2019, **2**, 600–606.

26 S. Fajardo, P. Ocón, J. L. Rodríguez and E. Pastor, Co Supported on N and S Dual-Doped Reduced Graphene Oxide as Highly Active Oxygen-Reduction Catalyst for Direct Ethanol Fuel Cells, *Chem. Eng. J.*, 2023, **461**, 142053.

27 S. A. Grigoriev, V. N. Fateev, A. S. Pushkarev, I. V. Pushkareva, N. A. Ivanova, V. N. Kalinichenko, M. Y. Presnyakov and X. Wei, Reduced Graphene Oxide and Its Modifications as Catalyst Supports and Catalyst Layer Modifiers for PEMFC, *Materials*, 2018, **11**, 1405.

28 M. Xu, L. Wu, M. Zhu, Z. Wang, Z.-H. Huang and M.-X. Wang, Self-Supporting Nitrogen-Doped Reduced Graphene Oxide@ Carbon Nanofiber Hybrid Membranes as High-Performance Integrated Air Cathodes in Microbial Fuel Cells, *Carbon*, 2022, **193**, 242–257.

29 M. A. Sheikh-Mohseni, V. Hassanzadeh and B. Habibi, Reduced Graphene Oxide Supported Bimetallic Ni–Co Nanoparticles Composite as an Electrocatalyst for Oxidation of Methanol, *Solid State Sci.*, 2019, **98**, 106022.

30 K. Rahmani and B. Habibi, NiCo Alloy Nanoparticles Electrodeposited on an Electrochemically Reduced Nitrogen-Doped Graphene Oxide/Carbon-Ceramic Electrode: A Low Cost Electrocatalyst towards Methanol and Ethanol Oxidation, *RSC Adv.*, 2019, **9**, 34050–34064.

31 T. Noor, S. Pervaiz, N. Iqbal, H. Nasir, N. Zaman, M. Sharif and E. Pervaiz, Nanocomposites of NiO/CuO Based MOF with RGO: An Efficient and Robust Electrocatalyst for Methanol Oxidation Reaction in DMFC, *Nanomaterials*, 2020, **10**, 1601.

32 G. Sonia Theres, G. Velayutham, P. Santhana Krishnan and K. Shanthi, Synergistic Impact of Ni–Cu Hybrid Oxides Deposited on Ordered Mesoporous Carbon Scaffolds as Non-Noble Catalyst for Methanol Oxidation, *J. Mater. Sci.*, 2019, **54**, 1502–1519.

33 L.-S. Yuan, Y.-X. Zheng, M.-L. Jia, S.-J. Zhang, X.-L. Wang and C. Peng, Nanoporous Nickel-Copper-Phosphorus Amorphous Alloy Film for Methanol Electro-Oxidation in Alkaline Medium, *Electrochim. Acta*, 2015, **154**, 54–62.

34 D. Wu, W. Zhang and D. Cheng, Facile Synthesis of Cu/NiCu Electrocatalysts Integrating Alloy, Core–Shell, and One-Dimensional Structures for Efficient Methanol Oxidation Reaction, *ACS Appl. Mater. Interfaces*, 2017, **9**, 19843–19851.

35 Z. Mardani and M. B. Gholivand, Improvement of Electrocatalytic Activity of Bimetal Sulfide of Ni-Cu by α-MnO2 for Methanol Oxidation, *J. Electroanal. Chem.*, 2022, **923**, 116822.

36 E. Urbańczyk, M. Wala, A. Blacha-Grzechnik, A. Stolarczyk, A. Maciej and W. Simka, Electrocatalytic Methanol Oxidation Using Ni–Co–Graphene Composite Electrodes, *Int. J. Hydrogen Energy*, 2021, **46**, 33272–33286.

37 N. I. Zaaba, K. L. Foo, U. Hashim, S. J. Tan, W.-W. Liu and C. H. Voon, Synthesis of Graphene Oxide Using Modified Hummers Method: Solvent Influence, *Procedia Eng.*, 2017, **184**, 469–477.

38 J. Liu, X. Wang, J. Liu, H. Li and H. Zhang, Improved Mechanical Properties of Ni-RGO/Cu Composites Prepared by Molecular-Level Mixing, *Appl. Phys. A*, 2022, **128**, 165.

39 M. Sadiq, A. Arya and A. L. Sharma, Dielectric Study of Polymer Nanocomposite Films for Energy Storage Applications, In *Proceedings of the Recent Trends in Materials and Devices: Proceedings ICRTMD 2015*, Springer, 2017, pp. 389–396.

40 S. S. Shojaeenezhad, M. Farbod and I. Kazeminezhad, Effects of Initial Graphite Particle Size and Shape on Oxidation Time in Graphene Oxide Prepared by Hummers' Method, *J. Sci.: Adv. Mater. Devices*, 2017, **2**, 470–475.

41 C.-C. Hu, H.-H. Yeh, C.-P. Hu, R. L. G. Lecaros, C.-C. Cheng, W.-S. Hung, H.-A. Tsai, K.-R. Lee and J.-Y. Lai, The Influence of Intermediate Layer and Graphene Oxide Modification on the CO2 Capture Efficiency of Pebax-GO/PDMS/PSf Mixed Matrix Composite Membranes, *J. Taiwan Inst. Chem. Eng.*, 2022, **135**, 104379.

42 A. Y. Lee, K. Yang, N. D. Anh, C. Park, S. M. Lee, T. G. Lee and M. S. Jeong, Raman Study of D* Band in Graphene Oxide and Its Correlation with Reduction, *Appl. Surf. Sci.*, 2021, **536**, 147990.

43 S. Li, Z. Niu, Y. Jiao, P. Jin, D. Yang, C. Bai, J. Liu, G. Li and Y. Luo, Preparation of Different Morphology Cu/GO Nanocomposites and Their Catalytic Performance for Thermal Decomposition of Ammonium Perchlorate, *RSC Adv.*, 2022, **12**, 22806–22814.

44 V. Kumari, S. Kaushal and P. P. Singh, Green Synthesis of a CuO/RGO Nanocomposite Using a Terminalia Arjuna

Bark Extract and Its Catalytic Activity for the Purification of Water, *Mater. Adv.*, 2022, **3**, 2170–2184.

45 N. T. Vuong Hoan, N. T. Anh Thu, H. Van Duc, N. D. Cuong, D. Quang Khieu and V. Vo, Fe 3 O 4/Reduced Graphene Oxide Nanocomposite: Synthesis and Its Application for Toxic Metal Ion Removal, *J. Chem.*, 2016, **2016**, 2418172.

46 F. Bayansal, B. Şahin, M. Yüksel, N. Biyikli, H. A. Çetinkara and H. S. Güder, Influence of Coumarin as an Additive on CuO Nanostructures Prepared by Successive Ionic Layer Adsorption and Reaction (SILAR) Method, *J. Alloys Compd.*, 2013, **566**, 78–82.

47 Abid, P. Sehrawat, S. S. Islam, P. Mishra and S. Ahmad, Reduced Graphene Oxide (RGO) Based Wideband Optical Sensor and the Role of Temperature, Defect States and Quantum Efficiency, *Sci. Rep.*, 2018, **8**, 3537.

48 K. Abdelkarem, R. Saad, A. M. Ahmed, M. I. Fathy, M. Shaban and H. Hamdy, Efficient Room Temperature Carbon Dioxide Gas Sensor Based on Barium Doped CuO Thin Films, *J. Mater. Sci.*, 2023, **58**, 11568–11584.

49 C. C. Ngetich, J. M. Mutua, P. G. Kareru, E. Murimi and K. Karanja, Synthesis and Characterization of Graphene Oxide and Graphene Nanomaterial for Fuel Cell Applications, In *Proceedings of the Proceedings of the Sustainable Research and Innovation Conference*, 2022, pp. 92–96.

50 B. Sawicki, E. Tomaszewicz, M. Piątkowska, T. Groń, H. Duda and K. Górny, Correlation between the Band-Gap Energy and the Electrical Conductivity in MPr2W2O10 Tungstates (Where M= Cd, Co, Mn), 2016.

51 D. P. Volanti, M. O. Orlandi, J. Andrés and E. Longo, Efficient Microwave-Assisted Hydrothermal Synthesis of CuO Sea Urchin-like Architectures via a Mesoscale Self-Assembly, *CrystEngComm*, 2010, **12**, 1696–1699.

52 Q. Zhao and H. J. Kulik, Where Does the Density Localize in the Solid State? Divergent Behavior for Hybrids and DFT+ U, *J. Chem. Theory Comput.*, 2018, **14**, 670–683.

53 H. B. Liu, L. Xiang and Y. Jin, Hydrothermal Modification and Characterization of Ni (OH) 2 with High Discharge Capability, *Cryst. Growth Des.*, 2006, **6**, 283–286.

54 L. Wang, K. Zhang, Z. Hu, W. Duan, F. Cheng and J. Chen, Porous CuO Nanowires as the Anode of Rechargeable Na-Ion Batteries, *Nano Res.*, 2014, **7**, 199–208.

55 T. Gao and B. P. Jelle, Paraotwayite-Type α-Ni (OH) 2 Nanowires: Structural, Optical, and Electrochemical Properties, *J. Phys. Chem. C*, 2013, **117**, 17294–17302.

56 L. Dong, Y. Chu and W. Sun, Controllable Synthesis of Nickel Hydroxide and Porous Nickel Oxide Nanostructures with Different Morphologies, *Chem.–Euro. J.*, 2008, **14**, 5064–5072.

57 M. Zayed, A. M. Ahmed and M. Shaban, Synthesis and Characterization of Nanoporous ZnO and Pt/ZnO Thin Films for Dye Degradation and Water Splitting Applications, *Int. J. Hydrogen Energy*, 2019, **44**, 17630–17648.

58 B. Akbari, M. P. Tavandashti and M. Zandrahimi, Particle Size Characterization of Nanoparticles–a Practical Approach, *Iran. J. Mater. Sci. Eng.*, 2011, **8**, 48–56.

59 M. Zayed, N. Nasser, M. Shaban, H. Alshaikh, H. Hamdy and A. M. Ahmed, Effect of Morphology and Plasmonic on Au/ ZnO Films for Efficient Photoelectrochemical Water Splitting, *Nanomaterials*, 2021, **11**, 2338.

60 M. Shaban, K. Abdelkarem and A. M. El Sayed, Structural, Optical and Gas Sensing Properties of Cu2O/CuO Mixed Phase: Effect of the Number of Coated Layers and (Cr+ S) Co-Doping, *Phase Transitions*, 2019, **92**, 347–359.

61 M. M. El-Nahass, Z. El-Gohary and H. S. Soliman, Structural and Optical Studies of Thermally Evaporated CoPc Thin Films, *Opt. Laser Technol.*, 2003, **35**, 523–531.

62 A. Raslan, L. S. Del Burgo, J. Ciriza and J. L. Pedraz, Graphene Oxide and Reduced Graphene Oxide-Based Scaffolds in Regenerative Medicine, *Int. J. Pharm.*, 2020, **580**, 119226.

63 A. M. Al-Enizi, M. Ubaidullah, J. Ahmed, H. Alrobei and S. M. Alshehri, Copper Nickel@ Reduced Graphene Oxide Nanocomposite as Bifunctional Electro-Catalyst for Excellent Oxygen Evolution and Oxygen Reduction Reactions, *Mater. Lett.*, 2020, **260**, 126969.

64 K. R. Chaturvedi and T. Sharma, Carbonated Polymeric Nanofluids for Enhanced Oil Recovery from Sandstone Reservoir, *J. Pet. Sci. Eng.*, 2020, **194**, 107499.

65 Z. Liu, Q. Wang, Q. Kong, X. Tong, S. Wu, N. Zong, R. Xu and L. Yang, One-Step Electrosynthesis of Bifunctional NiCu Nanosheets on Iron Foam for Remarkably Enhanced Alkaline Water Splitting, *Sustainability*, 2023, **15**, 12240.

66 A. B. Yousaf, S. A. M. Alsaydeh, F. S. Zavahir, P. Kasak and S. J. Zaidi, Ultra-Low Pt-Decorated NiCu Bimetallic Alloys Nanoparticles Supported on Reduced Graphene Oxide for Electro-Oxidation of Methanol, *MRS Commun.*, 2018, **8**, 1050–1057.

67 B. Ballarin, R. Seeber, D. Tonelli and A. Vaccari, Electrocatalytic Properties of Nickel (II) Hydrotalcite-Type Anionic Clay: Application to Methanol and Ethanol Oxidation, *J. Electroanal. Chem.*, 1999, **463**, 123–127.

68 E. E. Abdel-Hady, M. Shaban, M. O. Abdel-Hamed, A. Gamal, H. Yehia and A. M. Ahmed, Synthesis and Characterization of NiCoPt/CNFs Nanoparticles as an Effective Electrocatalyst for Energy Applications, *Nanomaterials*, 2022, **12**, 492.

69 Y. S. Li, T. S. Zhao and Z. X. Liang, Performance of Alkaline Electrolyte-Membrane-Based Direct Ethanol Fuel Cells, *J. Power Sources*, 2009, **187**, 387–392.

70 Z. Deng, Q. Yi, Y. Zhang and H. Nie, NiCo/CN/CNT Composite Catalysts for Electro-Catalytic Oxidation of Methanol and Ethanol, *J. Electroanal. Chem.*, 2017, **803**, 95–103.

71 N. A. M. Barakat, M. A. Yassin, F. S. Al-Mubaddel and M. T. Amen, New Electrooxidation Characteristic for Ni-Based Electrodes for Wide Application in Methanol Fuel Cells, *Appl. Catal., A*, 2018, **555**, 148–154.

72 J. Yang, Z. Ju, Z. Jiang, Z. Xing, B. Xi, J. Feng and S. Xiong, Enhanced Capacity and Rate Capability of Nitrogen/Oxygen Dual-doped Hard Carbon in Capacitive Potassium-ion Storage, *Adv. Mater.*, 2018, **30**, 1700104.

73 N. Elgrishi, K. J. Rountree, B. D. McCarthy, E. S. Rountree, T. T. Eisenhart and J. L. Dempsey, A Practical Beginner's

Guide to Cyclic Voltammetry, *J. Chem. Educ.*, 2018, **95**, 197–206.

74 A. Sood, A. D. Poletayev, D. A. Cogswell, P. M. Csernica, J. T. Mefford, D. Fraggedakis, M. F. Toney, A. M. Lindenberg, M. Z. Bazant and W. C. Chueh, Electrochemical Ion Insertion from the Atomic to the Device Scale, *Nat. Rev. Mater.*, 2021, **6**, 847–867.

75 S. Tamang, S. Rai, R. Bhujel, N. K. Bhattacharyya, B. P. Swain and J. Biswas, A Concise Review on GO, RGO and Metal Oxide/RGO Composites: Fabrication and Their Supercapacitor and Catalytic Applications, *J. Alloys Compd.*, 2023, 169588.

76 Y.-H. Mao, C.-Y. Chen, J.-X. Fu, T.-Y. Lai, F.-H. Lu and Y.-C. Tsai, Electrodeposition of Nickel-copper on Titanium Nitride for Methanol Electrooxidation, *Surf. Coat. Technol.*, 2018, **350**, 949–953.

77 Z. Li, Y. Yan, S.-M. Xu, H. Zhou, M. Xu, L. Ma, M. Shao, X. Kong, B. Wang and L. Zheng, Alcohols Electrooxidation Coupled with H2 Production at High Current Densities Promoted by a Cooperative Catalyst, *Nat. Commun.*, 2022, **13**, 147.

78 A. Parsa and S. Amanzadeh-Salout, Electrocatalytic Activity and Electrochemical Impedance Spectroscopy of Poly (Aniline-Co-Ortho-Phenylenediamine) Modified Electrode on Ascorbic Acid, *Orient. J. Chem.*, 2016, **32**, 2051.

79 L.-J. Feng, X.-H. Zhang, D.-M. Zhao and S.-F. Wang, Electrochemical Studies of Bovine Serum Albumin Immobilization onto the Poly-o-Phenylenediamine and Carbon-Coated Nickel Composite Film and Its Interaction with Papaverine, *Sens. Actuators, B*, 2011, **152**, 88–93.

80 S. Dhillon and R. Kant, Theory for Electrochemical Impedance Spectroscopy of Heterogeneous Electrode with Distributed Capacitance and Charge Transfer Resistance, *J. Chem. Sci.*, 2017, **129**, 1277–1292.

81 N. H. Helal, Corrosion Inhibition and Adsorption Behavior of Methionine on Mg-Al-Zn Alloy, *J. Chem. Eng. Mater. Sci.*, 2011, **2**, 28–38.

82 H. Tian, G. Zhao, Y. Zhang, Y. Wang and T. Cao, Hierarchical (0 0 1) Facet Anatase/Rutile TiO2 Heterojunction Photoanode with Enhanced Photoelectrocatalytic Performance, *Electrochim. Acta*, 2013, **96**, 199–205.

83 Y. Sun, T. Zhou, Q. Pan, X. Zhang and J. Guo, PtFe/Nitrogen-Doped Graphene for High-Performance Electrooxidation of Formic Acid with Composition Sensitive Electrocatalytic Activity, *RSC Adv.*, 2015, **5**, 60237–60245.

84 I. A. Khan, M. Sofian, A. Badshah, M. A. Khan, M. Imran and M. A. Nadeem, Stable and Efficient PtRu Electrocatalysts Supported on Zn-BTC MOF Derived Microporous Carbon for Formic Acid Fuel Cells Application, *Front. Chem.*, 2020, **8**, 367.

85 F.-M. Li, Y.-Q. Kang, H.-M. Liu, Y.-N. Zhai, M.-C. Hu and Y. Chen, Atoms Diffusion-Induced Phase Engineering of Platinum-Gold Alloy Nanocrystals with High Electrocatalytic Performance for the Formic Acid Oxidation Reaction, *J. Colloid Interface Sci.*, 2018, **514**, 299–305.

86 S. Y. Shen, T. S. Zhao, J. B. Xu and Y. S. Li, Synthesis of PdNi Catalysts for the Oxidation of Ethanol in Alkaline Direct Ethanol Fuel Cells, *J. Power Sources*, 2010, **195**, 1001–1006.

87 F.-K. Chen, Y.-H. Ho, H.-W. Chang and Y.-C. Tsai, Nanocomposite Integrating Tube-like NiCo2S4 and Carbon Nanotubes for Electrooxidation of Methanol, *Electrochem. Commun.*, 2020, **117**, 106783.

88 J. Hu, R. Li, X. Wang, S. Wang and C. Fang, Strain-Induced Porous Pd@ PdPt Core/Shell Nanocubes as Effective All-in-One Electrocatalysts toward Multialcohol Oxidation, *ACS Appl. Nano Mater.*, 2023, **6**(12), 10213–10222.

89 A. Higareda, F. Mares-Briones, G. Rosas, R. Pérez and R. Esparza, Enhanced Durability of Pdpt/c Electrocatalyst during the Ethanol Oxidation Reaction in Alkaline Media, *J. Solid State Electrochem.*, 2022, **26**, 2143–2151.

90 Q. Q. Xia, L. Y. Zhang, Z. L. Zhao and C. M. Li, Growing Platinum-Ruthenium-Tin Ternary Alloy Nanoparticles on Reduced Graphene Oxide for Strong Ligand Effect toward Enhanced Ethanol Oxidation Reaction, *J. Colloid Interface Sci.*, 2017, **506**, 135–143.

91 P. Li, K. Liu, J. Ye, F. Xue, Y. Cheng, Z. Lyu, X. Liao, W. Wang, Q. Zhang and X. Chen, Facilitating the C–C Bond Cleavage on Sub-10 Nm Concavity-Tunable Rh@ Pt Core–Shell Nanocubes for Efficient Ethanol Electrooxidation, *J. Mater. Chem. A*, 2019, **7**, 17987–17994.

92 Z. Han, A.-J. Wang, L. Zhang, Z.-G. Wang, K.-M. Fang, Z.-Z. Yin and J.-J. Feng, 3D Highly Branched PtCoRh Nanoassemblies: Glycine-Assisted Solvothermal Synthesis and Superior Catalytic Activity for Alcohol Oxidation, *J. Colloid Interface Sci.*, 2019, **554**, 512–519.

93 R. Ding, S. Zhang, Y. Chen, Z. Rui, K. Hua, Y. Wu, X. Li, X. Duan, X. Wang and J. Li, Application of Machine Learning in Optimizing Proton Exchange Membrane Fuel Cells: A Review, *Energy and AI*, 2022, **9**, 100170.

94 C. Zhao, S. Yuan, X. Cheng, Z. Zheng, J. Liu, J. Yin, S. Shen, X. Yan and J. Zhang, The Effect of Catalyst Layer Design on Catalyst Utilization in PEMFC Studied via Stochastic Reconstruction Method, *Energy and AI*, 2023, **13**, 100245.